EUROFUSION WP15ER-PR(16) 16343

E Strumberger et al.

CASTOR3D: Linear Stability Studies for 2D and 3D Tokamak Equilibria

Preprint of Paper to be submitted for publication in
Nuclear Fusion

This work has been carried out within the framework of the EUROfusion Consortium and has received funding from the Euratom research and training programme 2014-2018 under grant agreement No 633053. The views and opinions expressed herein do not necessarily reflect those of the European Commission.

CASTOR3D: Linear Stability Studies for 2D and 3D Tokamak Equilibria

E. Strumberger and S. Günter
Max Planck Institute for Plasma Physics, Boltzmannstr. 2.
85748 Garching, Germany

July 12, 2016

Abstract

The CASTOR3D code, which is currently under development, is able to perform linear stability studies for 2D and 3D, ideal and resistive tokamak equilibria in presence of ideal and resistive wall structures and coils. Solving an extended eigenvalue problem, the code takes simultaneously plasma inertia and wall resistivity into account. The CASTOR3D code is a hybrid of the CASTOR_3DW stability code and the STARWALL code. The former is an extended version of the CASTOR and CASTOR_FLOW code, respectively. The latter is a linear 3D code computing the growth rates of resistive wall modes in the presence of multiply-connected wall structures. The CASTOR_3DW code, and some parts of the STARWALL code have been reformulated in a general 3D flux coordinate representation that allows to choose between various types of flux coordinates. Furthermore, the implemented "Lüst Martensen term" in the STARWALL part allows to investigate vertical displacement events. In this paper, we outline the theoretical concept, and present some numerical results which illustrate the present status of the code and demonstrate its numerious application possibilities.

Keywords: MHD, linear stability, 3D resistive equilibria, flux coordinates, resistive wall modes, vertical displacement events.

email address of the corresponding author: ers@ipp.mpg.de (E. Strumberger)

1 Introduction

The axisymmetry of tokamaks is always disturbed by the toroidal field ripple and small error fields. However, this asymmetry is usually neglected in equilibrium and linear stability studies. The situation changes if resistive walls with a complex three-dimensional structure are installed in tokamaks. These wall structures reduce the growth rates of external modes to the resistive time scale, and, therefore, allow for feedback stabilization [1, 2]. But, being non-axisymmetric they also cause a coupling of the toroidal harmonics [3, 4, 5, 6]. Furthermore, 3D effects may be generated e.g. by asymmetrically placed Test Blanked Modules (TBMs) in ITER [7], and/or by additional external fields produced by Magnetic Perturbation (MP) coils. The latter are applied to mitigate or even to suppress Edge Localized Modes (ELMs) [8, 9]. TBMs and/or MP fields lead to a corruagtion of the magnetic flux surfaces up to ten times larger than the displacement caused by the field ripple. Therefore, such tokamak equilibria are to be considered three-dimensional [10].

The three-dimensional equilibrium geometry and/or the presence of 3D wall structures require the use of 3D stability codes. There are several 3D, ideal, linear stability codes, for example: CAS3D [11], TERPSICHORE [12], and STARWALL [5, 13]. The latter takes multiply-connected resistive wall structures into account. However, it neglects the plasma inertia and is, therefore, restricted to the study of resistive wall modes. Furthermore, these codes use straight field line coordinates, the so-called Boozer coordinates [14]. These coordinates work fine for stellarators, but they are not the best choice in the boundary region close to the separatrix of a tokamak equilibrium. There, the poloidal coordinate lines strongly bend towards the X-point and become almost parallel to the radial ones. That is, especially, in case of ELMs and resistive wall modes these coordinates may cause numerical problems.

So, the motivation to develop a new 3D linear code for stability studies of tokamak equilibria is manyfold. The CASTOR3D code, which is currently under development, shall be used for 2D and 3D linear stability studies including: (i) all relevant physics effects such as: plasma resistivity, plasma flow, diamagnetic drift, etc., (ii) the presence of coils and multiply-connected, ideal and resistive wall structures, (iii) the simultaneous consideration of plasma inertia and resistive wall effects. Using appropriate flux coordinates, the code should be able to handle stability studies of VDEs, external modes and ELMs.

The CASTOR3D code is a hybrid of the CASTOR_3DW stability code [15] and the STARWALL code [5]. The CASTOR_3DW code is an extended version of the CASTOR [16, 17], and the CASTOR_FLOW code [18], respectively. It uses the vacuum solution of the STARWALL code and takes the coupling of the toroidal harmonics caused by 3D wall structures

into account. However, this code version is restricted to axisymmetric equilibria and ideal wall structures. Therefore, the CASTOR_3DW code and some parts of the STARWALL code have been rewritten in a general 3D flux coordinate representation. This representation allows to choose between various types of flux coordinates, and to perfom linear stability studies of 2D and 3D, ideal and resistive tokamak equilibria. Additionally, the CASTOR3D code is able to solve an extended eigenvalue problem that takes plasma inertia and wall resistivity into account simultaneously. Furthermore, the implemented "Lüst Martensen term" [19] in the STARWALL part [5] allows to investigate Vertical Displacement Events (VDEs).

In Section 2 we present four test equilibria and their representation in different flux coordinate systems. These equilibria are used to illustrate the present status of the CASTOR3D code and to demonstrate its numerious application possibilities. Subject of Section 3 is the theoretical formulation of the plasma part (Sect. 3.1 and 3.2). Numerical results are presented for 2D and 3D, ideal (Sect. 3.3) and resistive (Sect. 3.4) internal modes. Properties of various flux coordinate systems are compared. Section 4 deals with the vacuum part of the CASTOR3D code. Boundary conditions (Sect. 4.1), and the two implemented methods for the computation of the vacuum response to unit perturbations, i.e. the solution of the Laplace equation (Sect. 4.2), and the variational method implemented in the STARWALL part (Sect. 4.3) are described. The various methods are benchmarked in Section 4.4. The merging of plasma and vacuum parts is subject of Section 5. The extended eigenvalue problem is formulated in Section 5.1, while results obtained for VDEs in presence of a resistive wall and ideal coils are presented in Section 5.2. Finally, in Section 6 a summary of the present code status, and an outlook to further extensions and improvements are given. The used coordinate systems, and the discretization of coil bands into triangles are described in more detail in the Appendices 1 and 2, respectively.

2 2D and 3D test equilibria

The two- and three-dimensional equilibria, which are the basis for the presented stability studies, are computed with the NEMEC code [20, 21]. This ideal equilibrium code relies on energy minimization, and assumes nested flux surfaces. Since the squared magnetic field, $\vec{B}_0^2$, is integrable, the radial differencing performed during the equilibrium calculation is insensitive to the singular behaviour of the current density at rational surfaces of 3D equilibria [22]. Therefore, no special treatment of rational surfaces, such as flattening of the pressure profile at these surfaces, is required. This is a very favourable property of the code, especially important in case of 3D tokamak equilibria which usually include a plenty of rational surfaces compared to

low-shear stellarators. The NEMEC code uses an optimized Fourier representation of the flux surfaces [23], with the latter labled by the normalized toroidal flux. As result, the code yields the Fourier spectra of the flux surfaces and the equilibrium magnetic field as smooth functions of the normalized toroidal flux. These Fourier spectra, or their transformation into straight field line coordinates, are used to compute the metric coefficients needed by the CASTOR3D code. However, although no singularities at rational surfaces have to be considered during the equilibrium or succeeding stability computations, one has to keep in mind that the assumed nested flux surfaces are only an approximation of the real equilibrium solution, which may contain islands or stochastic regions for 3D equilibria.

The numerious application possibilities of the CASTOR3D code, and the numerical accuracy of its results are verified using four different plasma equilibria. All equilibria are chosen with respect to their stability properties and the related numerical requirements, while their physical relevance plays a minor role here. Nevertheless, two of them (AUG-T1 and AUG-T2) are ASDEX Upgrade-type equilibria, in order to demonstrate the practicability of the CASTOR3D code with respect to realistic stability problems.

Table 1. Equilibrium properties

	unit	circle	ellipse	AUG-T1	AUG-T2
A		1.60	10.00	2.93	3.32
R_a	[m]	1.74	10.00	1.68	1.74
Z_a	[m]	0.00	0.00	0.10	0.07
p_a	[kPa]	337.50	1.00	106.30	189.10
B_a	[T]	0.93	2.25	2.91	2.32
I_p	[MA]	2.66	1.06	0.94	0.85
$< \beta >$	[%]	2.97	0.01	0.67	2.05

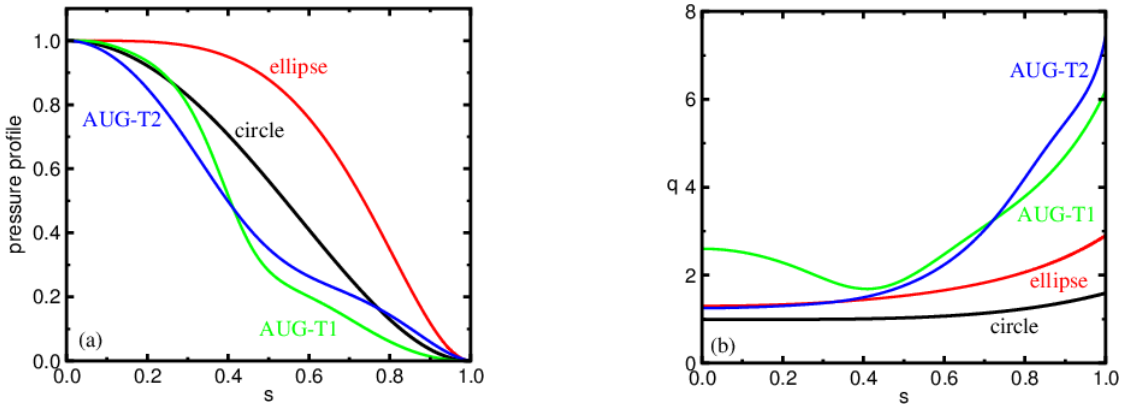

Fig. 1: (a) *Normalized pressure profiles, and (b) q-profiles of the four test equilibria as function of the square root of the normalized toroidal flux, s.*

In Table 1 physical properties of the considered equilibria are listed. There, A names the aspect ratio. $R_a,\ Z_a,\ p_a$ and B_a are R- and Z-coordinates, pressure and magnetic field strength at the magnetic axis. I_p names the toroidal plasma current, and $< \beta >$ is the volume averaged plasma-β. The corresponding pressure and q-profiles are shown in Fig. 1.

Assuming a plasma equilibrium solution with smooth and nested flux surfaces, the eigenvalue problem of the CASTOR3D code is formulated in a very general three-dimensional form using non-orthogonal flux coordinates (s, v, u). Here, the radial coordinate $s = \sqrt{\Phi}/\sqrt{\Phi_{max}}$ is defined as square root of the normalized toroidal flux (Φ_{max} is the total toroidal flux). The choice of the toroidal and poloidal, angle-like coordinates v and u is not fixed. However, they have to fulfil the following relations:

$$R(s,v,u) = \sum_{k=0,l=-l_{max}}^{k_{max},l_{max}} \hat{r}^c_{k,l}(s)\cos(2\pi(ku+lv)) + \hat{r}^s_{k,l}(s)\sin(2\pi(ku+lv)),$$

$$\varphi(s,v,u) = 2\pi v + 2\pi \sum_{k=0,l=-l_{max}}^{k_{max},l_{max}} \hat{v}^c_{k,l}(s)\cos(2\pi(ku+lv)) + \hat{v}^s_{k,l}(s)\sin(2\pi(ku+lv)), \quad (1)$$

$$Z(s,v,u) = \sum_{k=0,l=-l_{max}}^{k_{max},l_{max}} \hat{z}^c_{k,l}(s)\cos(2\pi(ku+lv)) + \hat{z}^s_{k,l}(s)\sin(2\pi(ku+lv)),$$

with the cylindrical coordinates (R, φ, Z) describing the flux surfaces labeled by s with $0 \leq s \leq 1$. The toroidal and poloidal coordinates are defined in the ranges $0 \leq v < 1$ and $0 \leq u < 1$. $\{\hat{r}^c_{kl}(s), \hat{r}^s_{kl}(s), \hat{v}^c_{kl}(s), \hat{v}^s_{kl}(s), \hat{z}^c_{kl}(s), \hat{z}^s_{kl}(s)\}$ are the Fourier coefficients representing the flux surfaces, with $0 \leq k \leq k_{max}$ and $-l_{max} \leq l \leq l_{max}$ being the poloidal and toroidal harmonics, respectively.

This general description of the flux surfaces is the basis for the formulation of the eigenvalue problem which also holds for 3D plasma equilibria. Here we use three different kinds of flux coordinates (see also Appendix 1): (i) flux coordinates used by the NEMEC equilibrium code [20, 21], (ii) straight field line coordinates used in the original CASTOR code [16, 17], which only hold for axisymmetric equilibria, and (iii) the so-called Boozer coordinates [14]. In Fig. 2 flux surfaces, and poloidal coordinate lines of the three coordinate systems are plotted for the four axisymmetric test equilibria. Due to the proximity of the chosen plasma boundary to the separatrix and the high q-value there, the poloidal coordinate lines of the straight field line and the Boozer coordinates become almost parallel to the radial ones in the boundary region of the AUG-T2 test equilibrium. Such a behaviour implies great numerical problems in the

computation of the metric elements. This can be avoided by using the NEMEC coordinates. These coordinates behave well everywhere, as also shown in Fig. 2.

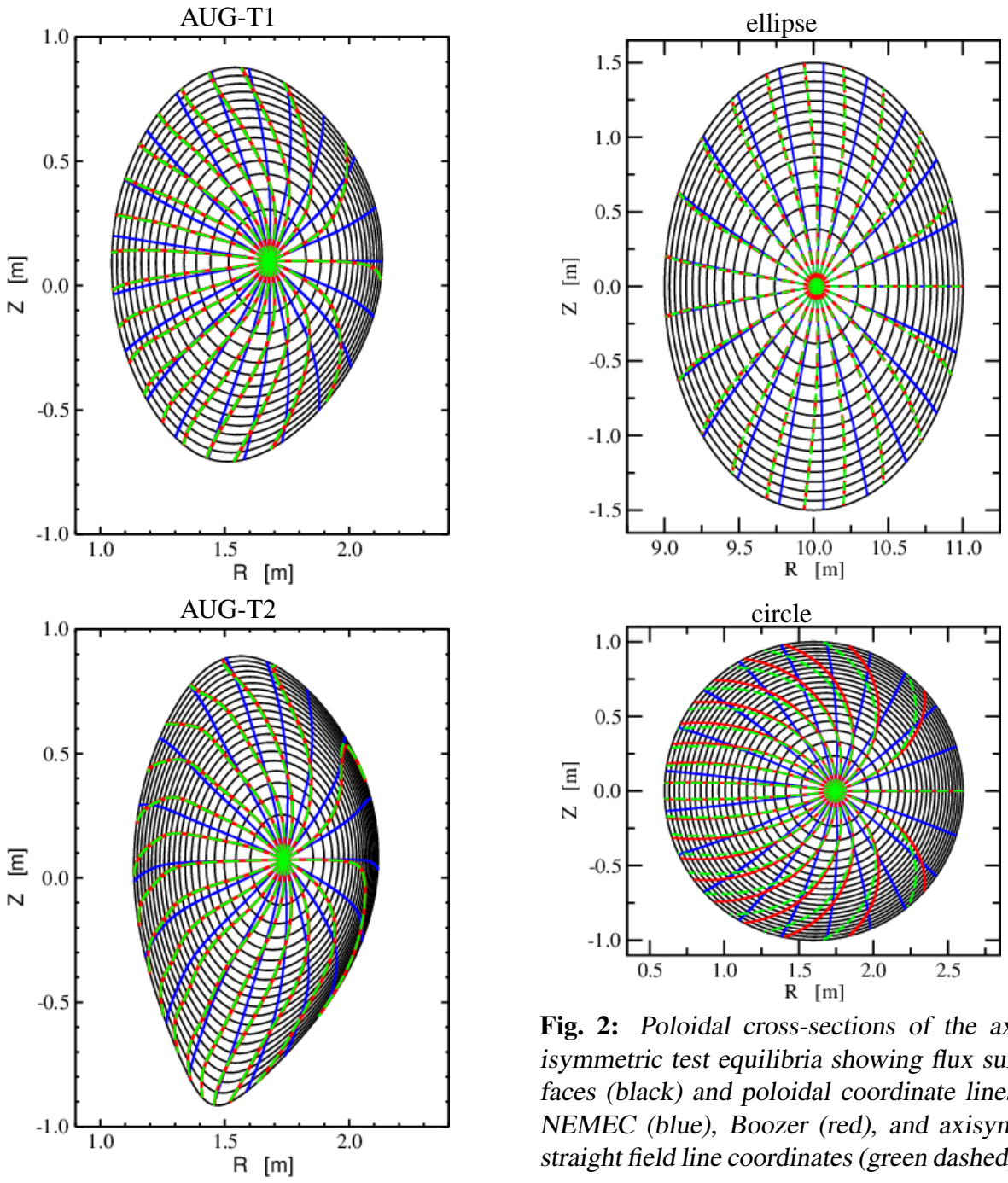

Fig. 2: *Poloidal cross-sections of the axisymmetric test equilibria showing flux surfaces (black) and poloidal coordinate lines: NEMEC (blue), Boozer (red), and axisym. straight field line coordinates (green dashed).*

All equilibria discussed above are axisymmetric equilibria. However, using the NEMEC code in its 3D mode (allowing for toroidal harmonics with $n \neq 0$), the circular equilibrium develops a helical core as will be described in Section 3.3. Furthermore, applying a 3D vacuum field

by taking the field of MP coils into account, a 3D equilibrium solution is obtained for test equilibrium AUG-T2 (see Sect.3.4).

3 Plasma part of the CASTOR3D code

3.1 Resistive, single-fluid MHD equations

The linear, resistive, single-fluid MHD equations read

$$\lambda\rho = -\vec{v}\cdot\nabla\rho_0 - \rho_0\nabla\cdot\vec{v}, \tag{2}$$

$$\lambda\rho_0\vec{v} = -\nabla(\rho_0 T + \rho T_0)/m + ((\nabla\times\vec{B}_0)\times\vec{B} + (\nabla\times\vec{B})\times\vec{B}_0)/\mu_0, \tag{3}$$

$$\lambda T = -\vec{v}\cdot\nabla T_0 - (\Gamma-1)T_0\nabla\cdot\vec{v}, \tag{4}$$

$$\lambda\vec{B} = \nabla\times(\vec{v}\times\vec{B}_0 - \eta\nabla\times\vec{B}/\mu_0), \tag{5}$$

with the time dependence of the perturbed quantities taken to be $\sim e^{\lambda t}$, and $\lambda = \gamma + i\omega$. The real part of λ denotes the growth rate, γ, while ω describes the oscillation frequency of the mode. The quantities ρ_0, T_0, and $\vec{B}_0$ are density, temperature, and magnetic field of the unperturbed equilibrium. The corresponding perturbed quantities are represented with the same symbols, but without zero. The compressibility of the plasma is described by the coefficient Γ, with $\Gamma = 5/3$ used here. The quantities m, μ_0, and η indicate particle mass, vacuum permeability, and plasma resistivity.

3.2 Weak formulation of the MHD equations

In case of the original CASTOR code the formulation of the eigenvalue problem has already been described in detail in [16, 17]. Here, only the most important steps are summarized including the extensions and modifications necessary for the 3D formulation in general flux coordinates.

The perturbed vector potential $\vec{A}$ is introduced by

$$\vec{B} = \nabla\times\vec{A} \quad \text{and} \quad \vec{E} = -\lambda\vec{A}, \tag{6}$$

where the scalar potential is set equal to zero because of the gauge invariance. This yields for (3) and (5)

$$\lambda\rho_0\vec{v} = -\nabla(\rho_0 T + \rho T_0)/m + ((\nabla\times\vec{B}_0)\times(\nabla\times\vec{A}) + (\nabla\times(\nabla\times\vec{A}))\times\vec{B}_0)/\mu_0 \tag{7}$$

and

$$\lambda\vec{A} = \vec{v}\times\vec{B}_0 - \frac{\eta}{\mu_0}\nabla\times(\nabla\times\vec{A}). \tag{8}$$

Analogous to the original CASTOR code a complex ansatz is made for the perturbed quantities

$$\rho = \frac{1}{s}\hat{\rho}, \quad T = \frac{1}{s}\hat{T}, \quad \vec{A} = -i\hat{A}_s\nabla s + \hat{A}_v\nabla v + \hat{A}_u\nabla u,$$

$$\vec{v} = v^s\vec{r}_{,s} + v^v\vec{r}_{,v} + v^u\vec{v}_{,u} = \frac{R^2}{\sqrt{g}}\hat{v}_s\vec{r}_{,s} + \frac{R^2}{i\iota\hat{f}}\hat{v}_v\vec{B}_0 + \frac{R^2}{i\sqrt{g}}\hat{v}_u\vec{r}_{,u}\,. \tag{9}$$

Here $\sqrt{g} = \vec{r}_{,s}\cdot(\vec{r}_{,v}\times\vec{r}_{,u})$ is the Jacobian, $\hat{f} = \partial\Phi/\partial s$ the derivative of the toroidal flux Φ, and ι the rotational transform. The equilibrium magnetic field, $\vec{B}_0$, is used in its covariant representation

$$\vec{B}_0 = B^u\vec{r}_{,u} + B^v\vec{r}_{,v}\,. \tag{10}$$

The eight variables $\hat{\rho}, \hat{v}_s, \hat{v}_u, \hat{v}_v, \hat{T}, \hat{A}_s, \hat{A}_u$ and $\hat{A}_v$ are collected in the state vector

$$\vec{w} = (\hat{\rho}, \hat{v}_s, \hat{v}_u, \hat{v}_v, \hat{T}, \hat{A}_s, \hat{A}_u, \hat{A}_v). \tag{11}$$

For its components, $\hat{w}_{\bar{f}}$, a general ansatz is made:

$$\hat{w}_{\bar{f}}(s,v,u) = \sum_{\bar{m},\bar{n},\bar{j},\bar{q}} a^{s,\bar{m},\bar{n}}_{\bar{f},\bar{j},\bar{q}} h^{\bar{j}}_{\bar{f},\bar{q}} \sin(2\pi(\bar{m}u + \bar{n}v)) + a^{c,\bar{m},\bar{n}}_{\bar{f},\bar{j},\bar{q}} h^{\bar{j}}_{\bar{f},\bar{q}} \cos(2\pi(\bar{m}u + \bar{n}v)). \tag{12}$$

It is a combination of Fourier series in poloidal and toroidal direction, and finite elements in radial direction. Using the e-function representation of the sine and cosine functions, the CASTOR compatible form

$$\hat{w}_{\bar{f}}(s,u,v) = \sum_{\bar{m},\bar{n},\bar{j},\bar{q}} c^{\bar{m},\bar{n}}_{\bar{f},\bar{j},\bar{q}} h^{\bar{j}}_{\bar{f},\bar{q}} e^{2\pi i(\bar{m}u+\bar{n}v)} + \bar{c}^{\bar{m},\bar{n}}_{\bar{f},\bar{j},\bar{q}} h^{\bar{j}}_{\bar{f},\bar{q}} e^{-2\pi i(\bar{m}u+\bar{n}v)} \tag{13}$$

is obtained, with $c^{\bar{m},\bar{n}}_{\bar{f},\bar{j},\bar{q}}$ and $\bar{c}^{\bar{m},\bar{n}}_{\bar{f},\bar{j},\bar{q}}$ being the resulting combinations of $a^{s,\bar{m},\bar{n}}_{\bar{f},\bar{j},\bar{q}}$ and $a^{c,\bar{m},\bar{n}}_{\bar{f},\bar{j},\bar{q}}$.

In order to build the weak form, the following test functions

$$t^{s,m,n}_{f,j,q}(s,v,u) = \hat{t}_f h^j_{f,q} \sin(2\pi(mu+nv)) = \hat{t}_f h^j_{f,q} \frac{1}{2i}\left(e^{2\pi i(mu+nv)} - e^{-2\pi i(mu+nv)}\right) \tag{14}$$

$$t^{c,m,n}_{f,j,q}(s,v,u) = \hat{t}_f h^j_{f,q} \cos(2\pi(mu+nv)) = \hat{t}_f h^j_{f,q} \frac{1}{2}\left(e^{2\pi i(mu+nv)} + e^{-2\pi i(mu+nv)}\right) \qquad (15)$$

are used with the $\hat{t}_f$ chosen as in the original CASTOR code:

$$\hat{t}_{\hat{\rho}} = \frac{1}{s}, \quad \hat{t}_{\hat{T}} = \frac{1}{s}, \quad \hat{t}_{\hat{A}_s} = i\nabla s, \quad \hat{t}_{\hat{A}_u} = \nabla u, \quad \hat{t}_{\hat{A}_v} = \nabla v$$

$$\hat{t}_{\hat{v}_s} = \frac{R^2}{\sqrt{g}}\vec{r}_{,s}\,, \quad \hat{t}_{\hat{v}_u} = \frac{iR^2}{\sqrt{g}}\vec{r}_{,u}\,, \quad \hat{t}_{\hat{v}_v} = \frac{iR^2}{\sqrt{g}}\vec{r}_{,u} - \frac{iJ}{4\pi^2\iota\hat{f}}\vec{r}_{,v} \qquad (16)$$

with J being the poloidal current. In (13,14) and (15) f and $\bar{f}$ lable the eight variables, $m, n, \bar{m}, \bar{n}$ the poloidal and toroidal Fourier harmonics, and $j, \bar{j}$ the radial grid points. The interpolating functions $h^j_{f,q}$ and $h^{\bar{j}}_{\bar{f},\bar{q}}$ are either quadratic ($f, \bar{f} = \hat{\rho}, \hat{v}_u, \hat{v}_v, \hat{T}, \hat{A}_s$) or cubic ($f, \bar{f} = \hat{v}_s, \hat{A}_u, \hat{A}_v$) Hermite polynomials, which in the following are named $h^j_q, h^{\bar{j}}_{\bar{q}}$ (quadratic) and $H^j_q, H^{\bar{j}}_{\bar{q}}$ (cubic), respectively. Furthermore, $q, \bar{q} = 1, 2$ label the two different quadratic and cubic Hermite polynomials at each radial grid point. For the definition of these polynomials, e.g. see [17].

Inserting the ansatz for the perturbed quantities (9,13) into the MHD equations (2,7,4,8), multiplying them from the left hand side with the appropriate test functions (14,15), expressing the equilibrium quantities in poloidal and toroidal direction by Fourier series, and, finally, integrating the resulting equations over the plasma volume, the non-hermitian eigenvalue problem

$$\lambda \mathbf{B}\vec{x} = \mathbf{A}\vec{x} \qquad (17)$$

with the eigenvector $\vec{x} = (\{c^{\bar{m},\bar{n}}_{\bar{f},\bar{j},\bar{q}}\}, \{\bar{c}^{\bar{m},\bar{n}}_{\bar{f},\bar{j},\bar{q}}\})$ is obtained.

Taking into account that the eigenvalues of two orthogonal solutions are not degenerated in case of asymmetric problems, this eigenvalue problem is twice as large as the axismmetric eigenvalue problem solved by the original CASTOR code. In case of 3D, asymmetric equilibria and/or in presence of asymmetric wall and coil structures, usually two instead of one eigenvalue are obtained for a mode [15, 5]. However, in case of axisymmetric or stellartor-symmetric configurations, the size of the eigenvalue problem can be reduced to the one solved in the original CASTOR code with $\vec{x} = (\{c^{\bar{m},\bar{n}}_{\bar{f},\bar{j},\bar{q}}\})$. Furthermore, the solution of this smaller eigenvalue problem is a good approximation as long as the difference beween the two eigenvalues resulting from a non-symmetric, 3D geometry is smaller or in the range of the achieved numerical accuracy. All computations presented in Sections 3 and 4 have been performed by solving the smaller eigenvalue problem, because either axisymmetry or stellartor-symmetry is fulfiled, or only weakly violated.

The boundary terms arising in the weak form are presented in Section 4. In the next two subsections, we will concentrate on fixed-boundary modes. Then the essential boundary conditions read at the magnetic axis

$$v^s(s=0)=0, \quad A_u(s=0)=0, \quad A_v(s=0)=0, \tag{18}$$

and at a perfectly conducting wall at the plasma boundary

$$v^s(s=1)=0, \quad A_u(s=1)=0, \quad A_v(s=1)=0. \tag{19}$$

3.3 Fixed-boundary, ideal modes

At first, we study ideal modes of axisymmetric equilibria. We start with a simple equilibrium with circular cross-section (equilibrium CIRCLE, see Table1). Due to its high β-value, flat q-profile, and high pressure gradient around $q = 1$, the equilibrium is unstable with respect to $n \geq 1$ ideal kink modes. Here, we present computations up to $n = 7$. The computations have been performed using various formulations and several coordinate systems: the general 3D coordinate formulation for NEMEC coordinates, Boozer coordinates and 2D straight field coordinates, as well as the original formulation of the CASTOR code based on 2D straight field coordinates. Additionally, the results are benchmarked with the CAS3DN code. This code is a slightly modified version of the CAS3D code [11] in which a non-equidistant radial grid has been implemented. As shown in Fig. 3a, the growth rates of the internal kink modes computed with different coordinates and codes agree very well within 0.5%. Note, here and in the following the corresponding CASTOR3D results obtained for NEMEC coordinates serve as reference points for the deviations given in per cent. In order to reach such a high accuracy, sufficient poloidal harmonics have to be taken into account. We have used 11 - 15 poloidal harmonics in case of NEMEC coordinates, and 17 - 23 harmonics otherwise. The number of poloidal harmonics increases with growing toroidal harmonic, n.

The number of contributing poloidal harmonics increases also with the complexity of the shaping of the poloidal plasma cross-section as illustrated in Fig. 3b. There, the growth rates of the $n = 3$ and $n = 5$ internal kink modes of the AUG-type equilibrium AUG-T2 are plotted as function of the total number of used poloidal harmonics, N_m. While the CASTOR3D results using NEMEC coordinates are already pretty well converged using less than 20 poloidal harmonics, at least 30 ($n = 3$ mode) or 40 ($n = 5$ mode) harmonics are needed if straight field line coordinates are used. Here, we consider growth rates as converged if they do not change

more than 1% by further increasing the number of used harmonics. The results obtained with different coordinates and codes agree within 0.25% and 3.5%, respectively. The largest deviations occur between CASTOR3D and CAS3DN results, particulary for the $n = 5$ mode. Due to the higher n, which implies a smaller mode width, and the lower eigenvalue, the numerical differences between both codes become more important. Especially the choice of the radial coordinate (CASTOR3D: $s = \sqrt{S}$, CAS3DN: S) plays a role.

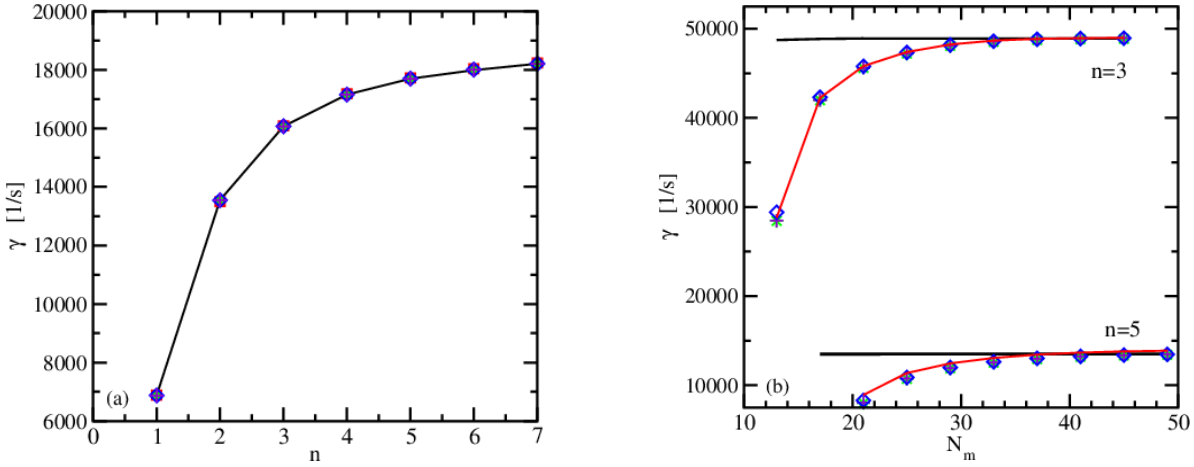

Fig. 3: *(a) Circular equilibrium: Growth rates of internal kink modes as function of the toroidal harmonic n. (b) AUG-T2 equilibrium: Growth rates of $n = 3$ and $n = 5$ internal kink modes as function of the total number of poloidal harmonics, N_m, which are taken into account. The black lines indicate the results obtained with the CASTOR3D code using NEMEC coordinates, while the red squares and lines, respectively, mark the CAS3DN results. The green stars denote the 2D straight field line coordinates using the original CASTOR formulation, while blue diamonds and violet plus signs show the results obtained with the general CASTOR3D formulation using 2D straight field line coordinates and Boozer coordinates, respectively.*

Doing a 3D NEMEC equilibrium calculation with axisymmetric plasma boundary and initial $m = 1, n = 1$ displacement of the magnetic axis for the circular equilibrium, a 3D equilibrium with helical core develops. The initial displacement of the magnetic axis numerically initiates the search for a non-axisymmetric solution, but has no influence on the final core size. As described in detail in [10], after returning to an almost axisymmetric solution a helical core develops, that is, the corrugation of the flux surfaces grows with increasing number of iterations until saturation. However, each of these iteration steps yields a quasi-equilibrium state with acceptably good numerical accuracy. Therefore, a set of equilibria which differ in the size of the helical deformation is available for the following stability studies.

Figure 4 shows the helical plasma core at the toroidal angles $\varphi = 0^{\circ}$ (black) and $\varphi = 180^{\circ}$ (red) after 120 000 iterations. The crosses mark the positions of the magnetic axis, while the green

dot represents the axis position of the axisymmetric equilibrium. Defining the radial shift, ΔR, of the magnetic axis at $\varphi = 0^{\circ}$ with respect to the axis position of the axisymmetric equilibrium as measure of the helical deformation, the plotted helical core corresponds to $\Delta R = 3.16$ cm.

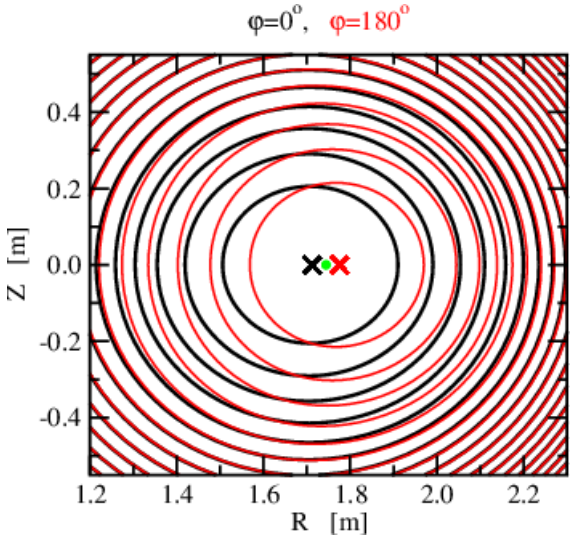

Fig. 4: *Poloidal cross-sections of the helical plasma core after 120 000 iterations at $\varphi = 0^{\circ}$ (black) and $\varphi = 180^{\circ}$ (red). The crosses mark the corresponding axis positions, while the green dot indicates the axis position of the axisymmetric equilibrium.*

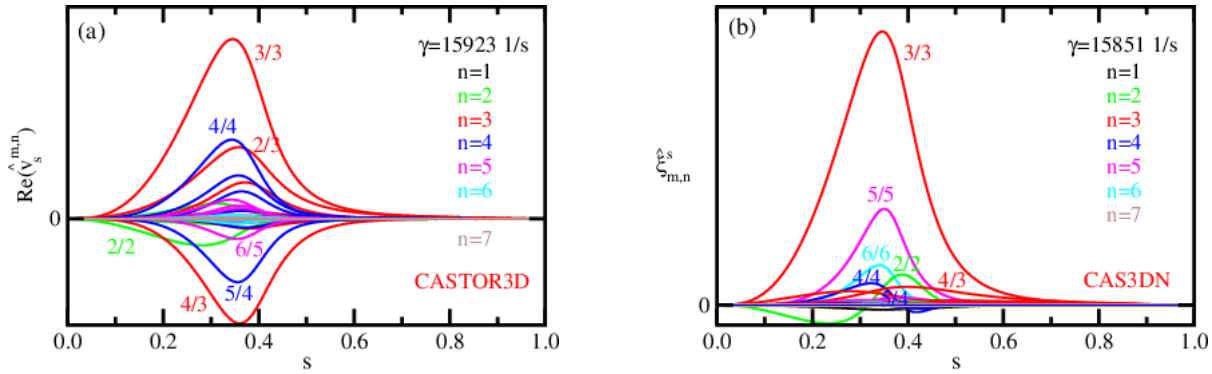

Fig. 5: *Eigenfunctions: (a) Real part of the Fourier spectrum of the radial velocity perturbation, $\hat{v}_s$, using NEMEC coordinates. (b) Corresponding Fourier spectrum, i.e. the radial displacement, $\hat{\xi}^s_{m,m}$, computed with the CAS3DN code using Boozer coordinates. Fourier coefficients of the same toroidal harmonic, n, are plotted with the same colour. The largest contributions are marked by their poloidal and toroidal harmonics, m/n.*

Since the helical deformation leads to a coupling of the toroidal harmonics, stability studies performed with the CAS3DN and the CASTOR3D codes yield several unstable modes. In Fig. 5, Fourier spectra of eigenfunctions belonging to the unstable mode with a dominant $n = 3$ character are presented for the equilibrium with $\Delta R = 3.16$ cm. Figure 5a shows the Fourier spectrum obtained with the CASTOR3D code using NEMEC coordinates, while Fig. 5b shows the spectrum computed with the CAS3DN code using Boozer coordinates. Since NEMEC coordinates are no straight field line coordinates, the dominant $m = 3$ character of the mode

is not as obvious from the Fourier spectrum as in case of Boozer coordinates. Therefore, we reconstructed the velocity perturbation from the Fourier spectrum of the CASTOR3D eigenfunctions. As shown in Fig. 6, the mode shows a clear $m = 3$ structure. Furthermore, the eigenvalues computed with both codes agree very well within 1% (see Fig. 5).

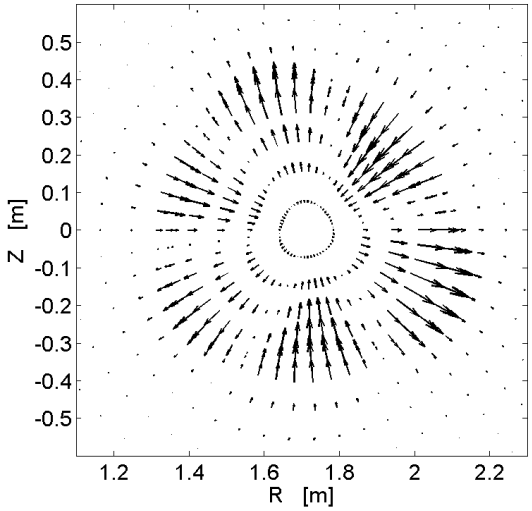

Fig. 6 *Mode structure of the internal kink mode with $\gamma = 15923$ 1/s. This mode shows a $m = 3$ structure. The vectors characterizing the velocity perturbation in the $R - Z$-plane are computed from the Fourier spectra of the corresponding eigenfunctions obtained with the CASTOR3D code using NEMEC coordinates.*

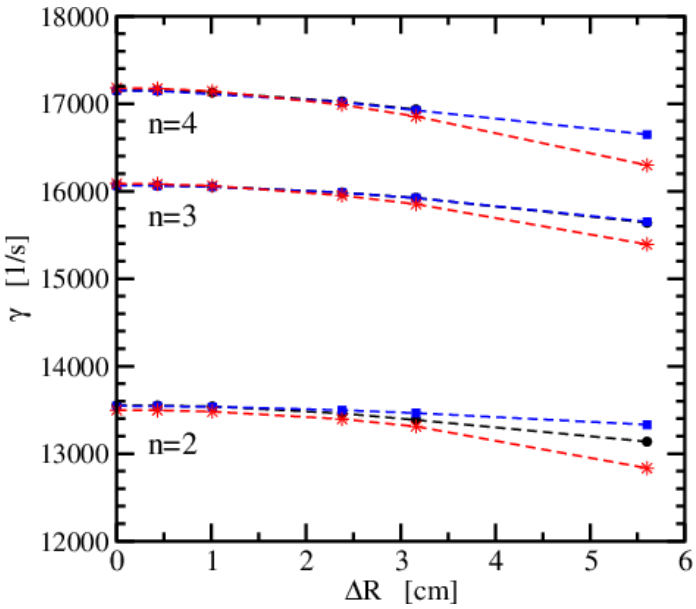

Fig. 7: *Growth rates of internal kink modes as function of the helical deformation of the plasma core, ΔR. n marks the main toroidal character of the mode. The CASTOR3D results are marked by black dashed lines/bullets (NEMEC coordinates) and blue dashed lines/squares (Boozer coordinates), while the CAS3DN results are given by red dashed lines/stars.*

As already mentioned, the helical deformation increases with the number of iterations. In Fig. 7 the growth rates of internal kink modes with dominant n=2,3 and 4 character are plotted as function of the helical deformation of the core, ΔR. The growth rates, which slightly decrease with increasing ΔR, are computed with the CASTOR3D code using NEMEC and Boozer coordinates, respectively, and with the CAS3DN code. For $\Delta R \leq 3.16$ cm the results agree within $\lesssim$1%, and even for $\Delta R \leq 5.6$ cm their deviation is still smaller than 4%. However, with increasing helical deformation the number of contributing poloidal and toroidal harmonics increases, while the numerical accuracy declines. In case of $\Delta R \leq 5.6$ cm already 95 (CASTOR3D, NEMEC coordinates) and 147 (CASTOR3D, Boozer coordinates, and CAS3DN) harmonics have been taken into account.

3.4 Fixed-boundary, resistive modes

The axisymmetric test equilibrium AUG-T1, which has a reversed q-profile (see Fig. 1b), is unstable with respect to a (2,1) Double Tearing Mode (DTM). This test equilibrium is used to benchmark the various coordinate systems implemented in the CASTOR3D code in case of resistive modes.

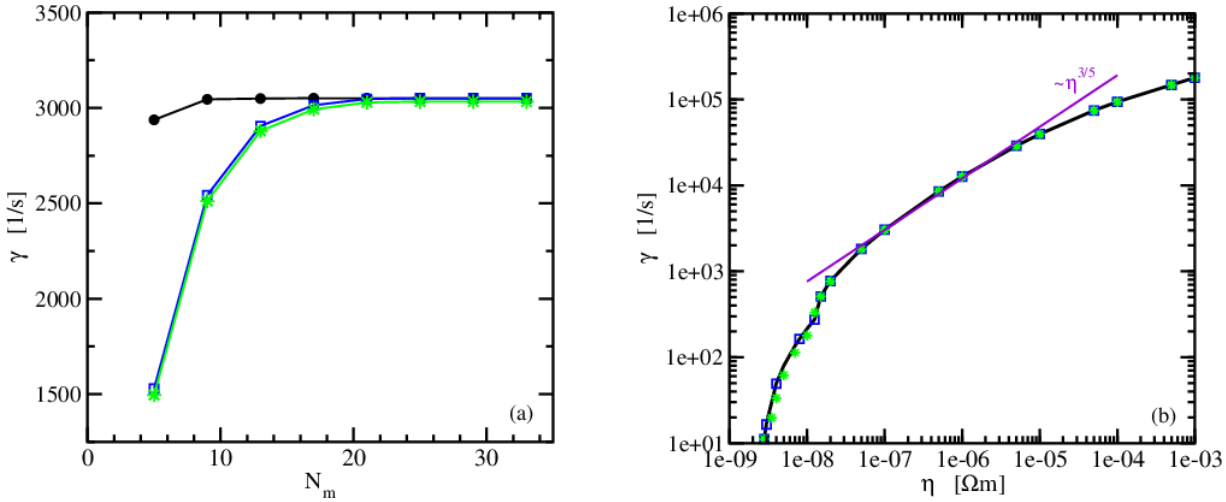

Fig. 8: *Benchmark between the CASTOR3D formulation in general 3D coordinates (NEMEC coordinates (black circles/line), Boozer coordinates (blue squares/line)) and its original formuluation in 2D straight field coordinates (green stars/line). (a) shows the dependence of the growth rate on the total number of poloidal Fourier harmonics, and (b) its dependence on the plasma resistivity.*

Choosing a constant plasma resistivity, $\eta = 1 \cdot 10^{-7}$ Ωm, we investigate the dependence of the DTM growth rate on the total number of poloidal harmonics taken into account. In order to obtain a converged result, again less poloidal harmonics are needed in case of NEMEC coordinates ($N_m = 9$) than in case of straight field line coordinates ($N_m = 21$), as shown in Fig. 8a. The converged results agree very well for all cases. They differ by less than 0.6%. Furthermore, the growth rates computed with NEMEC coordinates and straight field line coordinates, respectively, exhibit the same dependence on the plasma resistivity, as shown in Fig. 8b. In all cases the DTM stabilizes for $\eta \lesssim 2.5 \cdot 10^{-9}$ Ωm, and the growth rates follow the typical single tearing mode scaling ($\gamma \propto \eta^{3/5}$) in the range of $5 \cdot 10^{-8} < \eta < 1 \cdot 10^{-5}$ Ωm.

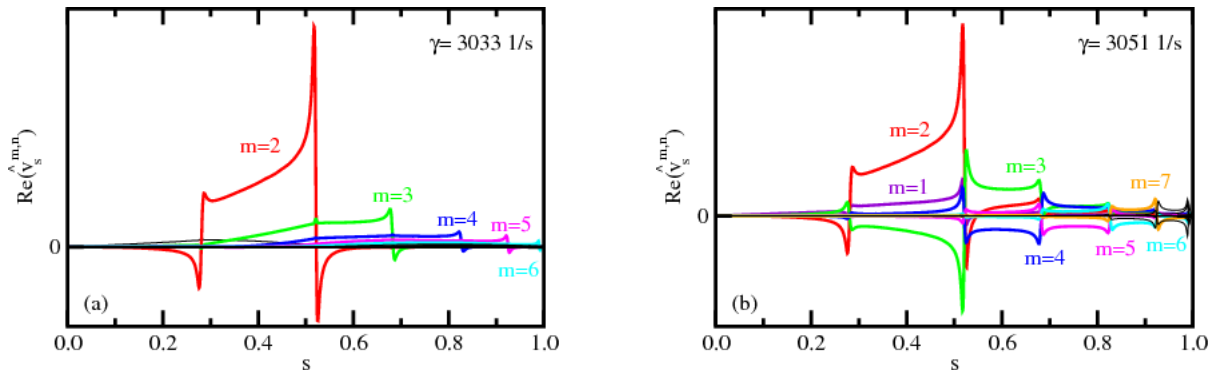

Fig. 9: *Fourier spectra of the eigenfunctions of the real part of the radial velocity perturbation in (a) straight field line coordinates (original 2D formulation), and (b) NEMEC coordinates.*

The Fourier spectra of the eigenfunctions of the real part of the radial velocity perturbation are shown in Fig.9 using straight field line coordinates in the original 2D formulation, and NEMEC coordinates. In both cases the Fourier harmonics change sign at rational surfaces as expected. However, using NEMEC coordinates, the harmonics change sign at every rational surface, while in case of straight field line coordinates, an m, n-harmonic only changes sign at the corresponding $q = m/n$ surface.

Finally, we study the effect of plasma resistivity on internal modes in case of a 3D, non-symmetric ASDEX Upgrade-type equilibrium. Turning on an $n = 2$ magnetic perturbation field, the AUG-T2 equilibrium becomes three-dimensional. Figure 10 shows the poloidal cross-sections of the axisymmetric equilibrium, which is unstable with respect to $n = 3$ and $n = 5$ internal kink modes (see Sect. 3.3, Fig. 3b), and the 3D equilibrium at $\varphi = 0^{\circ}$. Again, the 3D plasma geometry leads to a coupling of the toroidal harmonics. Since the corrugation of the flux surfaces is only of the order of 1 cm, merely 5 (NEMEC coordinates) to 7 toroidal harmonics (Boozer coordinates) contribute to the unstable ideal internal kink mode which is dominated by $n = 3$. The eigenvalues obtained with CAS3DN, CASTOR3D (Boozer coordinates), and

CASTOR3D (NEMEC coordinates) amount to 56023, 56355, and 57460 1/s, respectively. The CAS3DN code yields two eigenvalues (55869 1/s and 56023 1/s) which belong to the two orthogonal eigenfunctions. The eigenvalues of these two eigenfunctions split because the considered 3D equilibrium is not stellarator-symmetric. However, the difference between the two eigenvalues is too small to be found with the CASTOR3D code, which presently uses the inverse vector iteration method [24] for the solution of the eigenvalue problem. Therefore, we neglected this effect and solved the smaller eigenvalue problem as described in Sect. 3.2. It should be noted that, in contrast to the ideal CAS3DN code, the CASTOR3D code solves a non-hermitian eigenvalue problem.

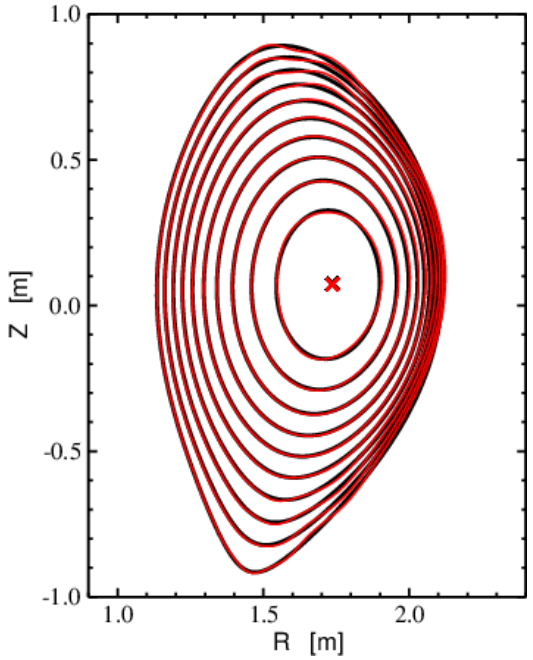

Fig. 10: *Poloidal cross-section of the axisymmetric equilibrium AUG-T2 (black), and the 3D equilibrium at $\varphi = 0^{\circ}$ (red). The latter is the result of an n=2 external perturbation field produced by the 16 MP coils implemented in ASDEX Upgrade [25].*

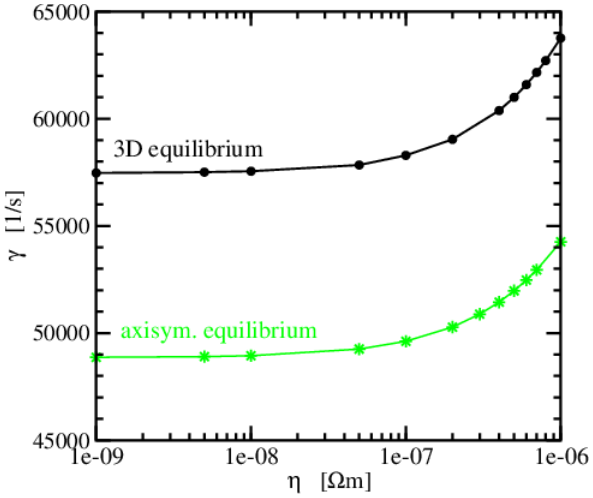

Fig. 11: *Growth rate as function of the plasma resistivity for the n=3 mode of the axisymmetric AUG-T2 equilibrium (green line/stars) and the corresponding mode of the 3D equilibrium (black line/circles).*

Using NEMEC coordinates, the growth rate of the $n = 3$ internal mode is determined as func-

tion of the plasma resistivity for the axisymmetric equilibrium, and analogous for the 3D equilibrium. Figure 11 shows a comparison of both cases. The growth rates possess the same dependence on η. However, the 3D equilibrium is more unstable due to the coupling of the toroidal harmonics. As shown in Fig. 12, it is mainly the coupling of $n = 3$ and $n = 5$ which makes the 3D equilibrium more unstable. Comparing the Fourier spectra obtained for the ideal plasma and for $\eta = 8 \cdot 10^{-7}$ Ωm, it seems that the contributions of the $n = 5$ harmonic slightly increase with the plasma resistivity.

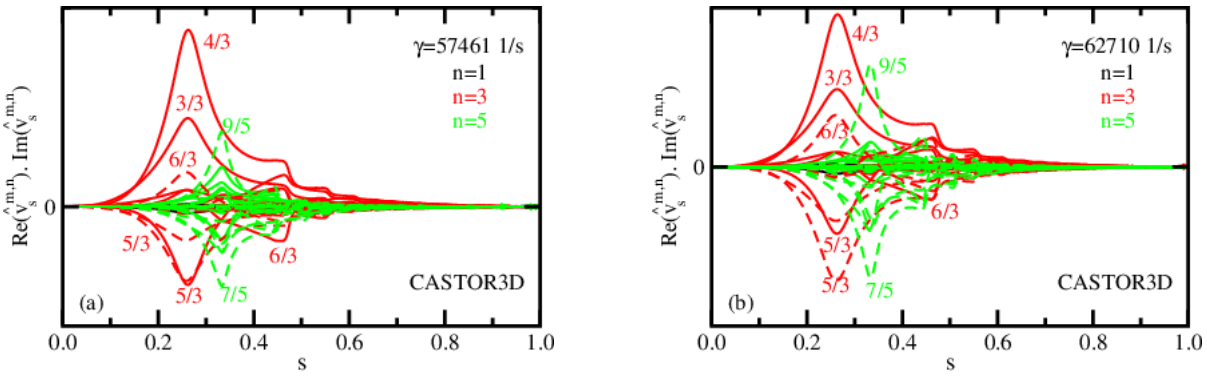

Fig. 12: *Real (solid lines) and imaginary parts (dashed lines) of the eigenfunction Fourier spectra of the radial velocity perturbation. (a) ideal, and (b) resistive plasma with* $\eta = 8 \cdot 10^{-7}$ Ωm.

4 Vacuum part of the CASTOR3D code

Free-boundary stability studies performed with the original CASTOR code are restricted to axisymmetric plasma surrounded by a vacuum domain and a closed, ideally conducting, axisymmetric wall located at some distance from the plasma [16]. Perturbing the vacuum with unit field perturbations at the plasma boundary, the vacuum response is determined by solving the weak form of the Laplace equation for each of these perturbations. Additionally to the solution of the Laplace equation, the variational method used in the STARWALL code [5] has been implemented in the CASTOR3D code. In contrast to the solution of the Laplace equation, this method also allows the computation of the vacuum response in case of no wall, and in presence of ideal coils and multiply-connected, ideal wall structures.

4.1 Boundary conditions

We consider only ideal equilibria without surface currents, i.e. the equilibrium field is continuous across the boundary, $\vec{B}_0 = \vec{B}_0^{vac}$, and the pressure p_0 goes to zero (see Fig. 1a). Then, in case of ideal stability studies ($\eta = 0$) the boundary conditions at the interface of an ideally conducting plasma and the surrounding vacuum are:

$$\vec{B} \cdot \vec{n}_p = \vec{B}^{vac} \vec{n}_p, \tag{20}$$

$$p + \vec{B}_0 \cdot \vec{B} = \vec{B}_0^{vac} \cdot \vec{B}^{vac}, \tag{21}$$

where $\vec{n}_p$ is the normal vector of the unperturbed plasma boundary, and $p = \rho_0 T + T_0 \rho$.

In case of resistive stability studies, surface currents are no longer allowed in the plasma perturbation. This leads to an additional condition

$$\vec{n}_p \times \vec{B} = \vec{n}_p \times \vec{B}^{vac}. \tag{22}$$

That is, also the tangential perturbations of the magnetic field, b_u and b_v, are continuous

$$\vec{B}_0 \cdot \vec{B} = \vec{B}_0^{vac} \cdot \vec{B}^{vac}, \tag{23}$$

and (21) reduces to $p = 0$ with the latter being satisfied via the chosen equilibria.

At the ideal wall the boundary condition simply reads

$$\vec{n}_w \cdot \vec{B}^{vac} = 0, \tag{24}$$

with $\vec{n}_w$ being the normal vector of the wall.

The CASTOR code [16, 17] makes use of a formulation where both the ideal and the resistive boundary conditions at the plasma-vacuum interface are implemented as natural boundary conditions, i.e. they are automatically satisfied when solving the weak form. In the CASTOR3D code this formulation is extended to 3D geometry and general flux coordinates.

The second-order derivatives in the radial coordinate arising in (7) and (8) can, in the weak form, be reduced to first-order derivatives by partial integration. Making use of the boundary conditions defined above, the weak formulation of the momentum equation (7) yields the boundary terms

$$W^s_{\hat{v}_s} = -\frac{1}{\mu_0} \int_0^1 \int_0^1 du dv H_q \sin(2\pi(mu + nv)) R^2 \vec{B}_0 \cdot \vec{B}^{vac})|_{s=1}, \tag{25}$$

$$W^c_{\hat{v}_s} = -\frac{1}{\mu_0}\int_0^1\int_0^1 dudv H_q \cos(2\pi(mu+nv))R^2\vec{B}_0\cdot\vec{B}^{vac})|_{s=1}. \tag{26}$$

The weak formulation of Ohm's law (8) leads to

$$W^s_{\hat{A}_u} = \frac{1}{\mu_0}\int_0^1 dv\int_0^1 du\; H_q \sin(2\pi(mu+nv))(-\eta)b^{vac}_v|_{s=1}, \tag{27}$$

$$W^c_{\hat{A}_u} = \frac{1}{\mu_0}\int_0^1 dv\int_0^1 du\; H_q \cos(2\pi(mu+nv))(-\eta)b^{vac}_v|_{s=1}, \tag{28}$$

$$W^s_{\hat{A}_v} = \frac{1}{\mu_0}\int_0^1 dv\int_0^1 du\; H_q \sin(2\pi i(mu+nv))\eta b^{vac}_u|_{s=1}, \tag{29}$$

$$W^c_{\hat{A}_v} = \frac{1}{\mu_0}\int_0^1 dv\int_0^1 du\; H_q \cos(2\pi i(mu+nv))\eta b^{vac}_u|_{s=1}. \tag{30}$$

The cubic Hermite polynomials are $H_1(s=1)=1$ and $H_2(s=1)=0$, that is, only terms with index $q=1$ do not vanish.

If the vacuum field is perturbed by unit perturbations at the plasma boundary, the vacuum magnetic field perturbation $\vec{B}^{vac} = b^{vac}_s\nabla s + b^{vac}_u\nabla u + b^{vac}_v\nabla v = \nabla\times\vec{A}^{vac}$ can be determined as function of these unit perturbations, in which the boundary condition (20) holds for each unit perturbation. In the following two subsections we will briefly describe the two methods that are implemented in the CASTOR3D code for determing the vacuum response.

4.2 Laplace equation

In the vacuum region between plasma and ideal wall, the perturbation of the magnetic field fulfils the relations $\nabla\times\vec{B}^{vac}=0$ and $\nabla\cdot\vec{B}^{vac}=0$. Using the first relation, it is possible to introduce a scalar magnetic potential Φ_M with $\vec{B}^{vac}=\nabla\Phi_M$. Then $\nabla\cdot\vec{B}^{vac}=0$ yields the Laplace equation

$$\Delta\Phi_M = 0. \tag{31}$$

Multiplying this equation with a test function t_k, and integrating over the vacuum region between plasma boundary and ideal wall gives its weak form

$$\int_{V_{vac}} \nabla t_k \Delta\Phi_M dV =$$

$$\int_{S_p} t_k \nabla\Phi_M \cdot \vec{n}_p dS + \int_{S_w} t_k \nabla\Phi_M \cdot \vec{n}_p dS - \int_{V_{vac}} \nabla t_k \cdot \nabla\Phi_M dV = 0. \tag{32}$$

The surface integrals are performed over the plasma boundary, S_p, and the ideal wall, S_w. Because of the boundary conditions (20) and (24) we obtain

$$\int_{V_{vac}} \nabla t_k \cdot \nabla\Phi_M dV = \int_{S_p} t_k (\vec{B}^{vac} \cdot \vec{n}_p) dS = \int_{S_p} t_k \sqrt{g} b^s du dv. \tag{33}$$

For Φ_M and $\sqrt{g}b^s$ Fourier ansatz are made

$$\Phi_M = \sum_{\bar{m}_v, \bar{n}_v, \bar{j}_v, \bar{q}} \phi^{s,\bar{m}_v,\bar{n}_v}_{\bar{j}_v,\bar{q}} H^{\bar{j}_v}_{\bar{q}} \sin(2\pi(\bar{m}_v u + \bar{n}_v v)) + \phi^{c,\bar{m}_v,\bar{n}_v}_{\bar{j}_v,\bar{q}} H^{\bar{j}_v}_{\bar{q}} \cos(2\pi(\bar{m}_v u + \bar{n}_v v)), \tag{34}$$

$$\sqrt{g}b^s = \sum_{\bar{m}_v, \bar{n}_v, \bar{j}_v, \bar{q}} d^{s,\bar{m}_v,\bar{n}_v}_{\bar{j}_v,\bar{q}} H^{\bar{j}_v}_{\bar{q}} \sin(2\pi(\bar{m}_v u + \bar{n}_v v)) + d^{c,\bar{m}_v,\bar{n}_v}_{\bar{j}_v,\bar{q}} H^{\bar{j}_v}_{\bar{q}} \cos(2\pi(\bar{m}_v u + \bar{n}_v v)). \tag{35}$$

As test functions, t_k, we choose

$$t^{s,m_v,n_v}_{\Phi_M,j_v,q} = H^{j_v}_q \sin(2\pi(m_v u + n_v v)), \quad t^{c,m_v,n_v}_{\Phi_M,j_v,q} = H^{j_v}_q \cos(2\pi(m_v u + n_v v)). \tag{36}$$

Inserting (34) and (35) into (33), and multiplying the resulting equation with the test functions (36) yields a set of linear equations. It reads in matrix form

$$\mathbf{E}\vec{c} = \vec{d} \tag{37}$$

with $\vec{c} = (\{\phi^{s,\bar{m}_v,\bar{n}_v}_{\bar{j}_v,\bar{q}}\}, \{\phi^{c,\bar{m}_v,\bar{n}_v}_{\bar{j}_v,\bar{q}}\})$ and $\vec{d} = (\{d^{s,\bar{m}_v,\bar{n}_v}_{\bar{j}_v,\bar{q}}\}, \{d^{c,\bar{m}_v,\bar{n}_v}_{\bar{j}_v,\bar{q}}\})$.

This linear equation system is solved separately for every unit perturbation

$$\vec{d}_{\bar{m},\bar{n}} = (..., 1, ...). \tag{38}$$

The latter is defined by 1 at position $\bar{m}, \bar{n}$ (sine or cosine component), and 0 otherwise. The solutions yield the magnetic potential Φ_M and, thereby, the perturbed magnetic field, $\vec{B}^{vac} = \nabla\Phi_M$, as functions of the unit perturbations.

In the CASTOR3D code this method has also been implemented for NEMEC coordinates, but up to now for axisymmetric geometry only.

4.3 Variational method

The STARWALL code [5] uses a variational method. For ideal wall and coil structures, the latter are considered as passive conductors, the Lagrangian reads

$$\mathcal{L}_{ideal} = \frac{\mu_0}{8\pi} \sum_{i,i'=1}^{2,2} \int_{S_i} df_i \int_{S_{i'}} df_{i'} \frac{\vec{K}_i \cdot \vec{K}_{i'}}{|\vec{r}_i - \vec{r}_{i'}|} - \int_{S_p} df_p \vec{K}_p \cdot \vec{A}^{vac} \tag{39}$$

$$+\frac{\mu_0}{8\pi} \sum_{n_c,n_c'=1}^{N_c,N_c} I_{n_c} I_{n_c'} \int_{S_{n_c}} df_{n_c} \int_{S_{n_c'}} df_{n_c'} \frac{\vec{k}_{n_c} \cdot \vec{k}_{n_c'}}{|\vec{r}_{n_c} - \vec{r}_{n_c'}|} + \frac{\mu_0}{4\pi} \sum_{n_c,i=1}^{N_c,2} I_{n_c} \int_{S_{n_c}} df_{n_c} \int_{S_i} df_i \frac{\vec{K}_i \cdot \vec{k}_{n_c}}{|\vec{r}_i - \vec{r}_{n_c}|}.$$

Here, the indices $i, i' = 1, 2$ mark the quantities related to the plasma boundary ($1 \widehat{=} p$) and the wall ($2 \widehat{=} w$), respectively, while index $n_c = 1, ..., N_c$ numbers the coils. $\vec{k}_{n_c}$ is the normalized surface current density, and I_{n_c} denotes the magnitude of the coil current of coil n_c. The divergence-free surface current densities

$$\vec{K}_i = \vec{n}_i \times \nabla \Phi^i \tag{40}$$

generate the magentic field perturbation in the vacuum domain, where Φ^i are the current potentials. Inserting (40) into the boundary term of the Lagrangian (39), making a partial integration, inserting $\vec{B}^{vac} = \nabla \times A^{vac}$ and $\vec{n}_p = \sqrt{g} \nabla s / |\vec{r}_{,v} \times \vec{r}_{,u}|$, and using the boundary condition (20), leads to

$$-\int_{S_p} df_p \vec{K}_p \cdot \vec{A}^{vac} = -\int_{S_p} df_p (\vec{n}_p \times \nabla \Phi^p) \cdot \vec{A}^{vac} = \int_{S_p} du dv \Phi^p |\vec{r}_{,v} \times \vec{r}_{,u}| (\vec{n}_p \cdot \vec{B}^{vac})$$

$$= \int_{S_p} du dv \Phi^p \sqrt{g} \nabla s \cdot \vec{B} = \int_{S_p} du dv \Phi^p \sqrt{g} b^s. \tag{41}$$

For $\sqrt{g} b^s$ we made again the ansatz (35). Fourier ansatz are also made for the current potential of the plasma boundary and the current potential of a closed wall with smooth geometry

$$\Phi^i(u, v) = \sum_{m_i, \bar{n}_i} \hat{\Phi}^{i,s}_{m_i,n_i} \sin(2\pi(m_i u + n_i v)) + \hat{\Phi}^{i,c}_{m_i,n_i} \cos(2\pi(m_i u + n_i v)) \tag{42}$$

where $i = p, w$. Coils and walls with complex, multiply-connected structure are discretized using triangles. Then the surface current density, $\vec{K}_\Delta$, is assumed to be constant on a triangle, and is defined by the values of the current potential at its vertices (for details see [5] and Appendix 2). However, here we consider only closed walls in Fourier representation, and coils discretized into triangles.

Inserting (40,41) and the ansatz (35,42) into the Lagrangian (39), and making the variation with respect to $\hat{\Phi}^{i,s}_{\bar{m},\bar{n}}$, $\hat{\Phi}^{i,c}_{\bar{m},\bar{n}}$ and I_{n_c}, the following linear equation system is obtained:

$$\begin{pmatrix} \mathbf{M}_{pp} & \mathbf{M}_{pw} & \mathbf{M}_{pc} \\ \mathbf{M}_{wp} & \mathbf{M}_{ww} & \mathbf{M}_{wc} \\ \mathbf{M}_{cp} & \mathbf{M}_{cw} & \mathbf{M}_{cc} \end{pmatrix} \cdot \begin{pmatrix} \vec{x}_p \\ \vec{x}_w \\ \vec{x}_c \end{pmatrix} = \begin{pmatrix} \mathbf{R}_{pd} \\ 0 \\ 0 \end{pmatrix} \cdot \vec{d}. \tag{43}$$

The matrices $\mathbf{M_{pp}}$, $\mathbf{M_{pw}}$, $\mathbf{M_{ww}}$ result from the first, $\mathbf{M_{cc}}$ from the third, $\mathbf{M_{pc}}$, $\mathbf{M_{wc}}$ from the forth, and $\mathbf{R_{pd}}$ from the boundary term of the Lagrangian. The symbolic vectors $\vec{x}_p = (\{\hat{\phi}^{p,s}_{m_p,n_p}\}, \{\hat{\phi}^{p,c}_{m_p,n_p}\})$, $\vec{x}_w = (\{\hat{\phi}^{w,s}_{\bar{m}_w,n_w}\}, \{\hat{\phi}^{w,c}_{m_w,n_w}\})$, and $\vec{x}_c = (\{I_{n_c}\})$ represent the Fourier coefficients of Φ^p, Φ^w, and the coil currents. Analogous to the solution of the Laplace equation, this linear equation system is solved for every unit perturbation (38) yielding the current potentials and the coil currents, and thereby the vacuum magnetic field perturbation

$$\vec{B}^{vac} = \vec{B}^{vac}_p + \vec{B}^{vac}_w + \sum_{n_c} \vec{B}^{vac}_{n_c} = \frac{\mu_0}{4\pi} \int_{S_p} df_p \vec{K}_p \times \frac{(\vec{r} - \vec{r}_p)}{|\vec{r} - \vec{r}_p|^3} + \frac{\mu_0}{4\pi} \int_{S_p} df_w \vec{K}_w \times \frac{(\vec{r} - \vec{r}_w)}{|\vec{r} - \vec{r}_w|^3}$$

$$+ \frac{\mu_0}{4\pi} \sum_{n_c}^{N_c} I_{n_c} \int_{S_{n_c}} df_{n_c} \vec{k}_{n_c} \times \frac{(\vec{r} - \vec{r}_{n_c})}{|\vec{r} - \vec{r}_{n_c}|^3} \tag{44}$$

as function of the unit perturbations.

4.4 Free-boundary DTM in presence of an ideal wall

The two solution methods discussed above are benchmarked for a free-boundary DTM in presence of an ideal, closed wall. The latter being shaped as the plasma boundary. Again the computations are performed for the AUG-T1 test equilibrium using a constant plasma resisitivity with $\eta = 1 \cdot 10^{-7}\Omega$m. Expanding the wall distance from almost zero to $r_w \geq 0.6$ m, the growth rate increases from the fixed-boundary value to the no wall limit. Here and in the following the distance between plasma boundary and wall, r_w, is measured at the low field side at the height of the magnetic axis, Z_a. Note that the configuration without wall can only be handled with the variational method, while the solution of the Laplace equation always requires a limiting wall. Using NEMEC coordinates and 2D straight field line coordinates, respectively, the growth rates obtained with the two solution methods excellently agree for $r_w > 2$ cm. The deviations of the results caused by the two solution methods are even smaller than the differences resulting from the general 3D and the original 2D straight field line formulation.

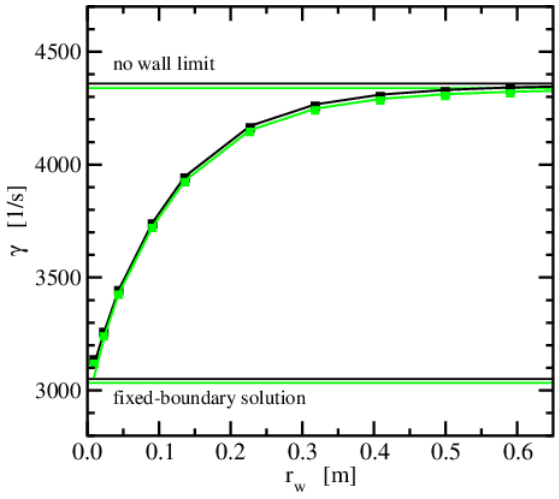

Fig. 14: *Growth rate of the DTM (AUG-T1 equilibrium, plasma resistivity $\eta = 1 \cdot 10^{-7}\Omega m$) as function of the wall distance, r_w. Results obtained with the two solution methods (lines: variational method, squares: solution of the Laplace equation) are compared using NEMEC coordinates (black) and 2D straight field line coordinates (green), respectively.*

5 Merging of plasma and vacuum parts

5.1 Formulation of the extended eigenvalue problem

In the presence of resistive wall and/or coil sturctures a further boundary condition has to be defined. Assuming an exponential time dependence, $e^{\lambda t}$, and using the thin wall approximation, the boundary condition for the perturbed vector potential [5] reads

$$\vec{n}_w \times \vec{A}^{vac} = -\frac{1}{\sigma_w d_w \lambda} \vec{n}_w \times \vec{K}_w \tag{45}$$

where σ_w and d_w are the specific wall resistivity and wall width, respectively. The dependency of this boundary condition on the eigenvalue λ suggests the formulation of an extended eigenvalue problem.

The Lagrangian including resistive wall and coil structures is defined by

$$\mathcal{L} = \mathcal{L}_{ideal} + \frac{1}{2\lambda\sigma_w d_w} \int_{S_w} df_w \vec{K}_w \cdot \vec{K}_w + \frac{1}{2\lambda} \sum_{n_c=1}^{N_c} R_{n_c} I_{n_c}^2 \int_{S_{n_c}} df_{n_c} \vec{k}_{n_c}^2 \tag{46}$$

with R_{n_c} being the resistance of coil n_c. Using the boundary condition for the vector potential at the plasma-vacuum interface

$$\vec{n}_p \times \vec{A}^{vac} = -(\vec{n}_p \cdot \vec{\xi}) \vec{B}_0, \tag{47}$$

the boundary term of $\mathcal{L}_{ideal}$ (39) is expressed by

$$\int_{S_p} df_p \vec{K}_p \cdot \vec{A}^{vac} = -\int_{S_p} df_p (\vec{n}_p \cdot \vec{\xi}) \vec{n}_p \cdot (\vec{K}_p \times \vec{B}_0) = -\frac{1}{\lambda} \int_{S_p} df_p (\vec{n}_p \cdot \vec{v}) \vec{n}_p \cdot (\vec{K}_p \times \vec{B}_0). \quad (48)$$

Here, we used the relation between displacement vector $\vec{\xi}$, velocity perturbation $\vec{v}$, and eigenvalue λ

$$\vec{\xi} = \frac{\vec{v}}{\lambda}. \quad (49)$$

In case of a vertical mode net-toroidal, I_p^T, I_w^T, and net-poloidal, I_p^P, I_w^P, currents are flowing on the plasma boundary and the plasma-facing surface of an ideal, closed wall [19]. The Fourier ansatz for the current potentials (42) (see Sect. 4.3) does not include these currents, and it therefore has to be extended to

$$\Phi^i = I_i^T u + I_i^P v + \sum_{m_i,n_i} \hat{\phi}^{i,s}_{m_i,n_i} \sin(2\pi(m_i u + n_i v)) + \sum_{m_i,n_i} \hat{\phi}^{i,c}_{m_i,n_i} \cos(2\pi(m_i u + n_i v)). \quad (50)$$

The variation of the Lagrangian with respect to $I_p^T, I_p^P, \hat{\Phi}^{p,s}_{m_p,n_p}, \Phi^{p,c}_{m_p,n_p}, I_w^T, I_w^P, \hat{\Phi}^{w,s}_{m_w,n_w}, \hat{\Phi}^{w,c}_{m_w,n_w}$, and I_{n_c} yields the equation system

$$\begin{pmatrix} \mathbf{M}_{pp} & \mathbf{M}_{pw} & \mathbf{M}_{pc} \\ \mathbf{M}_{wp} & \mathbf{M}_{ww} & \mathbf{M}_{wc} \\ \mathbf{M}_{cp} & \mathbf{M}_{cw} & \mathbf{M}_{cc} \end{pmatrix} \cdot \begin{pmatrix} \vec{x}_p \\ \vec{x}_w \\ \vec{x}_c \end{pmatrix} = -\frac{1}{\lambda} \begin{pmatrix} \mathbf{R}_{pd} & \mathbf{0}_{pp} & \mathbf{0}_{pw} & \mathbf{0}_{pc} \\ \mathbf{0}_{ws} & \mathbf{0}_{wp} & \mathbf{R}_{ww} & \mathbf{0}_{wc} \\ \mathbf{0}_{cs} & \mathbf{0}_{cp} & \mathbf{0}_{cw} & \mathbf{R}_{cc} \end{pmatrix} \cdot \begin{pmatrix} \vec{x}_d \\ \vec{x}_p \\ \vec{x}_w \\ \vec{x}_c \end{pmatrix} \quad (51)$$

for the vacuum region which has to be closed with equations derived for the plasma. Therefore, the eigenvalue problem (17) resulting form the MHD equations (2-5) is formulated in the following way

$$\lambda \begin{pmatrix} \mathbf{B}_{ll} & \mathbf{B}_{ld} \\ \mathbf{B}_{dl} & \mathbf{B}_{dd} \end{pmatrix} \begin{pmatrix} \vec{x}_l \\ \vec{x}_d \end{pmatrix} = \begin{pmatrix} \mathbf{A}_{ll} & \mathbf{A}_{ld} & \mathbf{0}_{lp} & \mathbf{0}_{lw} & \mathbf{0}_{lc} \\ \mathbf{A}_{dl} & \mathbf{A}_{dd} & \mathbf{R}_{dp} & \mathbf{R}_{dw} & \mathbf{R}_{dc} \end{pmatrix} \begin{pmatrix} \vec{x}_l \\ \vec{x}_d \\ \vec{x}_p \\ \vec{x}_w \\ \vec{x}_c \end{pmatrix}. \quad (52)$$

Here, the indices l and d characterize plasma interior and boundary related elements, respectively. The matrices $\mathbf{R}_{dp}$, $\mathbf{R}_{dw}$, and $\mathbf{R}_{dc}$ are obtained by inserting the definition of the magnetic field perturbation (44) into the boundary terms (25-29).

Finally, equations (51) and (52) are combined to the extended eigenvalue problem

$$\lambda \begin{pmatrix} \mathbf{B}_{ll} & \mathbf{B}_{ld} & \mathbf{0}_{lp} & \mathbf{0}_{lw} & \mathbf{0}_{lc} \\ \mathbf{B}_{dl} & \mathbf{B}_{dd} & \mathbf{0}_{dp} & \mathbf{0}_{dw} & \mathbf{0}_{dc} \\ \mathbf{0}_{pl} & \mathbf{0}_{pd} & \mathbf{M}_{pp} & \mathbf{M}_{pw} & \mathbf{M}_{pc} \\ \mathbf{0}_{wl} & \mathbf{0}_{wd} & \mathbf{M}_{wp} & \mathbf{M}_{ww} & \mathbf{M}_{wc} \\ \mathbf{0}_{cl} & \mathbf{0}_{cd} & \mathbf{M}_{cp} & \mathbf{M}_{cw} & \mathbf{M}_{cc} \end{pmatrix} \begin{pmatrix} \vec{x}_l \\ \vec{x}_d \\ \vec{x}_p \\ \vec{x}_w \\ \vec{x}_c \end{pmatrix} =$$

$$\begin{pmatrix} \mathbf{A}_{ll} & \mathbf{A}_{ld} & \mathbf{0}_{lp} & \mathbf{0}_{lw} & \mathbf{0}_{lc} \\ \mathbf{A}_{dl} & \mathbf{A}_{dd} & \mathbf{R}_{dp} & \mathbf{R}_{dw} & \mathbf{R}_{dc} \\ \mathbf{0}_{pl} & -\mathbf{R}_{pd} & \mathbf{0}_{pp} & \mathbf{0}_{pw} & \mathbf{0}_{pc} \\ \mathbf{0}_{wl} & \mathbf{0}_{wd} & \mathbf{0}_{wp} & -\mathbf{R}_{ww} & \mathbf{0}_{wc} \\ \mathbf{0}_{cl} & \mathbf{0}_{cd} & \mathbf{0}_{cp} & \mathbf{0}_{cw} & -\mathbf{R}_{cc} \end{pmatrix} \begin{pmatrix} \vec{x}_l \\ \vec{x}_d \\ \vec{x}_p \\ \vec{x}_w \\ \vec{x}_c \end{pmatrix} . \tag{53}$$

This eigenvalue problem includes the plasma and the vacuum region, in which the latter may also contain resistive wall and coils structures. Because of (i) the formulation of (53) in general 3D flux coordinates, (ii) the possibility of representing wall and coil structures by triangles, and (iii) the inclusion of physical effects, such as plasma resistivity, plasma flow, and diamagnetic drift (the implementation of the latter two is in progress) make the CASTOR3D code a very flexible and powerful numerical tool for linear stability studies of 2D and 3D tokamak equilibria.

5.2 VDEs and resistive walls

The elliptical equilibrium described in Sect. 2 is unstable with respect to a vertical displacment event. We use this equilibrium surrounded by a vacuum region, a closed, elliptically-shaped resistive wall and 16 ideally conducting, toroidal field coils to study the growth rate of a VDE as function of the wall distance. Here, the toroidal field coils allow for the net-poloidal current, I_w^P (50), which appears in case of a $m = 0, n = 0$ harmonic. However, the net-toroidal current, I_w^T flowing on an ideal wall, can be neglected, because it does not contribute to the magnetic field in the region enclosed by this wall. The CASTOR3D results are benchmarked with results obtained with the CAS3DN and the STARWALL codes. Furthermore, the computations are performed using two different density profiles. That is, a constant density, and a density profile corresponding to the square root of the pressure profile of the elliptical equilibrium are used. Since the density at the magnetic axis is assumed to be the same in both cases, the plasma inertia is higher in case of the constant density.

First of all, the growth rates obtained without a wall are computed with the CASTOR3D code. These no-wall limits are marked with red and black horizontal lines in Fig. 15a. As a consequence of the higher inertia, the growth rate is smaller in case of the constant density. Then, the growth rates as function of the distance of an ideal wall are determined with the CAS3DN code using the vacuum solution provided by the STARWALL code. In Fig. 15 these results are marked by the green (density profile) and violet (constant density) solid lines/plus signs. As expected, the growth rates converge against the corresponding no-wall limit with growing wall distance. The growth rates exhibit an almost singular decrease, and become independent of the plasma inertia (see Fig. 15a and 15b) when the wall distance approximates the ideal wall limit,

that is, the distance when the mode becomes stabilized by the ideal wall. For wall distances smaller than the ideal wall limit, the STARWALL code is used to determine the growth rate of the resistive wall mode marked by blue plus signs in Fig. 15. Finally, the CASTOR3D code is used to compute the growth rate as function of a resistive wall (red and black solid lines/bullets) over the whole distance range. In case of small wall distances the results agree very well with the STARWALL results (see Fig. 15c), while for large distances the wall resistivity plays no role, and the CASTOR3D results approximate the CAS3DN results (see Fig. 15a) obtaind for an ideal wall. However, in an intermediate range, where plasma inertia and wall resistivity have to be taken into account simultaneously, only the CASTOR3D code provides a growth rate by solving the extended eigenvalue problem desribed in the previous section. These results are shown in detailed in Fig. 15b.

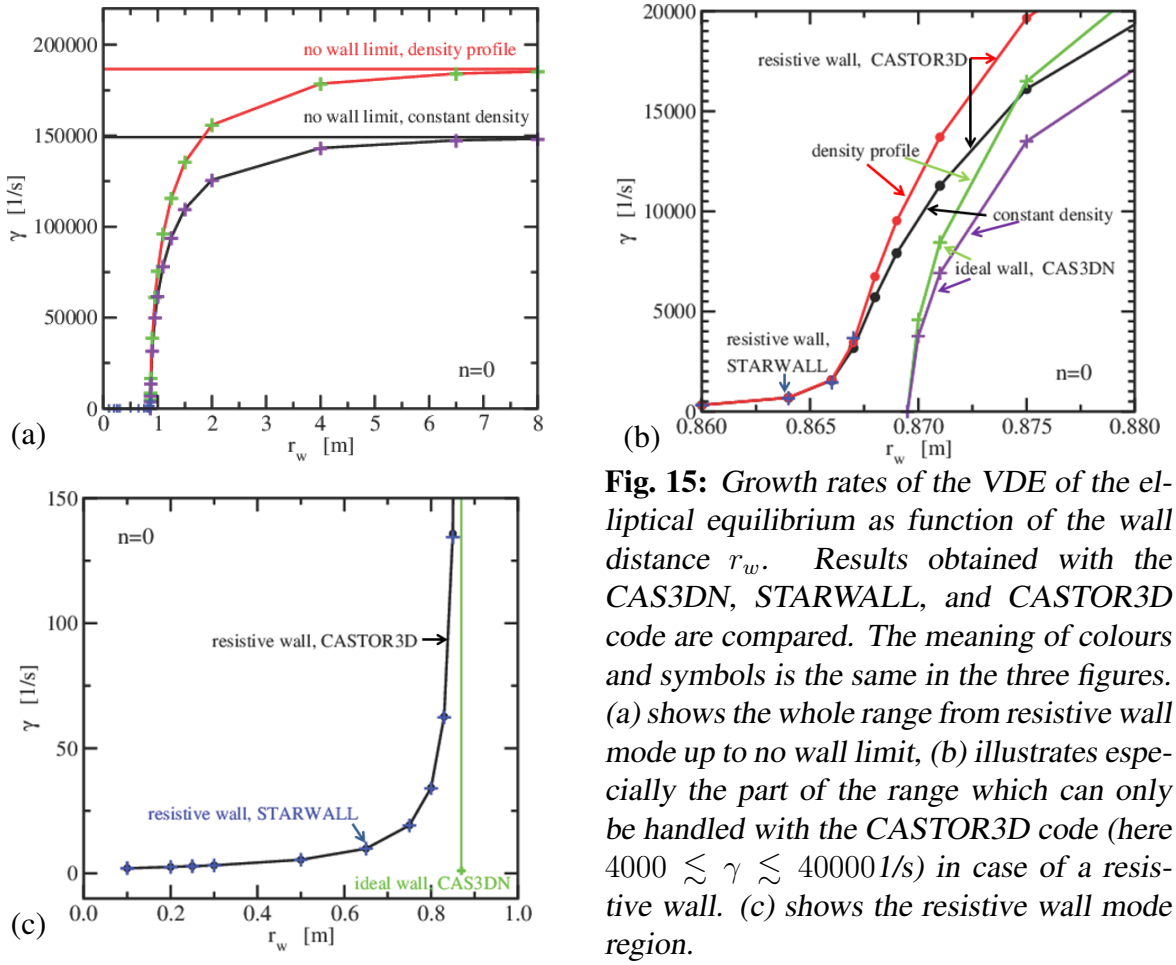

Fig. 15: *Growth rates of the VDE of the elliptical equilibrium as function of the wall distance r_w. Results obtained with the CAS3DN, STARWALL, and CASTOR3D code are compared. The meaning of colours and symbols is the same in the three figures. (a) shows the whole range from resistive wall mode up to no wall limit, (b) illustrates especially the part of the range which can only be handled with the CASTOR3D code (here $4000 \lesssim \gamma \lesssim 40000$1/s) in case of a resistive wall. (c) shows the resistive wall mode region.*

In case of no wall and a constant density profile, the VDE mode structures shown in Fig. 16 have been obtained with the CASTOR3D code. The two vector plots illustrate the velocity perturbation for the elliptical equilibrium (Fig. 16a) and the 3D AUG-T2 equilibrium (Fig. 16b). The mode structure of the elliptical equilibrium represents very well the downward shift of a

rigid body, as it is expected for such a symmetric equilibrium. The situation is slightly different in case of the AUG-T2 equilibrium. There is also a shift of the whole plasma. However, the shift is largest close to the plasma boundary at the low field side, and the vectors do not point exactly in vertical direction. In both cases, the mode structures reveal a high quality of the eigenfunctions. The eigenvalues amount to $\gamma = 149197$ 1/s and $\gamma = 453570$ 1/s, respectively. It should also be mentioned that in case of the 3D AUG-T2 equilibrium the torodial coupling of $n = 0$ with higher n-harmonics has been neglected. First of all, due to the large growth rate of the VDE and the small 3D deformation of the plasma, a very weak coupling is expected. Secondly, the efficiency of the CASTOR3D code has to be further improved (e.g. parallelization of the code), since the total number of harmonics contributing to such a problem, would largely exceed the number of harmonics taken into account in case of the fixed-boundary mode in Sect. 3.4.

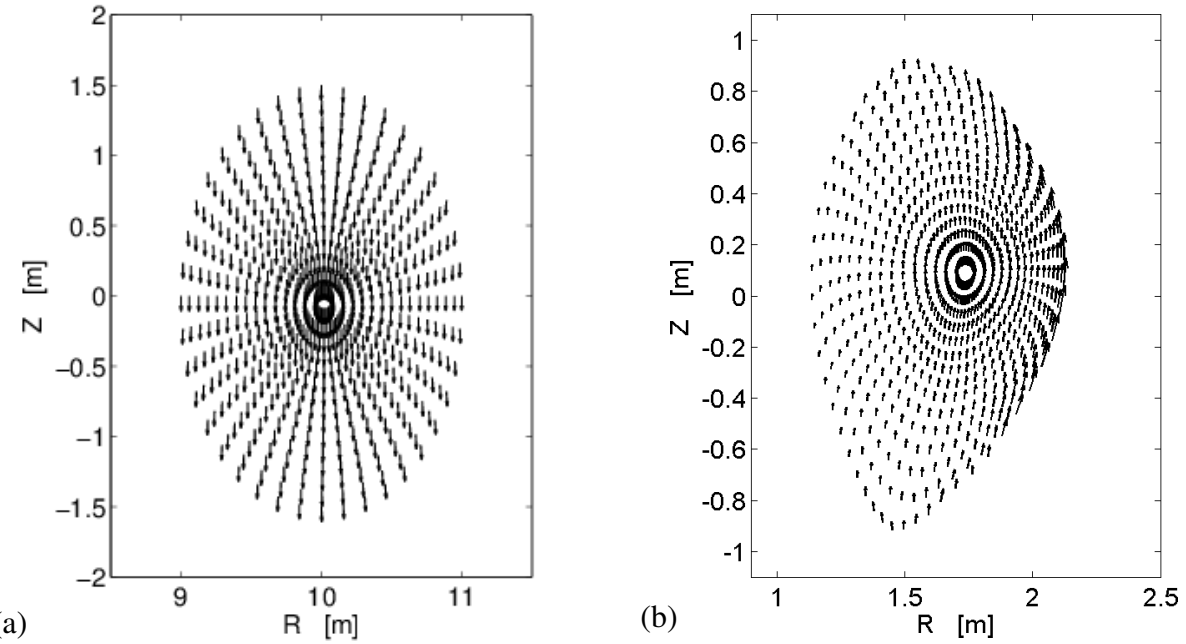

Fig. 16: *Mode structure of the VDE of (a) the elliptical equilibrium, and (b) the 3D AUG-T2 equilibrium. The vectors characterize the velocity perturbation in the R-Z plane at* $\varphi = 0^{\circ}$.

6 Summary and outlook

In this paper we presented an overview of the theoretical background and various application possiblities of the new 3D, resistive, linear stability code CASTOR3D. This code is based on the combination of the CASTOR_3DW code, and the STARWALL code. Numerous modifications

and extensions of both code parts led to a synergistic effect. That is, the number of possible applications of the CASTOR3D code exceeds easily the possibilities of both of them. The code has a number of significant advantages. It allows: (i) to choose between various kinds of flux coordinates, (ii) to perform stability studies for 3D, ideal and resistive tokamak equilibria, (iii) to take simultaneously into account plasma inertia and resistive walls, (iv) to investigate Vertical Displacement Events, and (v) to deal with coils and multiply-connected wall structures.

The presented benchmark calculations showed an excellent agreement between the CASTOR3D results and the results obtained with the CAS3DN code, the STARWALL code, and the previous CASTOR version. The latter is restricted to axisymmetric equilibria and straight field line coordinates. Several of the CASTOR3D computations were performed for NEMEC, Boozer, and 2D straight field line coordinates. All the results obtained using these coordinates agree very well. Furthermore, they show that an appropriate choice of the coordinates may noticeably reduce the number of required poloidal and toroidal harmonics, and, therefore, reduce computing time and memory. For the presented examples, the NEMEC coordinates are the better choice.

In contrast to straight field line coordinates, the NEMEC coordinates behave well in the boundary region. Therefore, using these coordinates for the stability studies of ELMs and external kink modes, we expect less numerical problems and a higher accuracy.

The CASTOR3D code still needs extensions, e.g. the implementation of plasma flow, diamagnetic drift, etc., and numerical improvements. The latter concern the parallelization of the code and the use of an efficient, parallelized eigenvalue solver for non-hermitian eigenvalue problems. A parallel eigenvalue solver of the Scalable Library for Eigenvalue Problem Computations (SLEPc) [26], is currently being implemented.

Acknowlegements

The authors would like to thank Peter Merkel, Karl Lackner, Carolin Nührenberg and Jürgen Nührenberg for useful discussions.

This work has been carried out within the framework of the EUROfusion Consortium and has received funding from the Euratom research and training programme 2014-2018 under grant agreement number 633053. The views and opinions expressed herein do not necessarily reflect those of the European Commission.

References

[1] CHU, M. S. and OKABAYASHI, M., Plasma Phys. Control. Fusion **52** (2010) 123001.

[2] SEMPF, M., MERKEL, P., STRUMBERGER, E., TICHMANN, C., and GÜNTER, S., New J. Phys. **11** (2009) 053015.

[3] STRUMBERGER, E., MERKEL, P., SEMPF, M., and GÜNTER, S., Phys. Plasmas **15** (2008) 056110.

[4] MERKEL, P., NÜHRENBERG, C., and STRUMBERGER, E., Resistive wall modes of 3D equilibria with multiply-connected walls, in *31st EPS Conf. on Contr. Fusion and Plasma Phys.*, ECA Vol. 28G P-1.208, London, UK, 2004.

[5] MERKEL, P. and STRUMBERGER, E., *Linear MHD stability studies with the STARWALL code*, http://arxiv.org/abs/1508.04911, 2015.

[6] LIU, Y., CHU, M. F., GUO, W. F., et al., Plasma Phys. Control. Fusion **52** (2010) 104002.

[7] SHINOHARA, K., KURKI-SUONIO, T., SPONG, D., et al., Nuclear Fusion **51** (2011) 063028.

[8] EVANS, T. E., FENSTERMACHER, M. E., MOYER, R. A., et al., Nuclear Fusion **48** (2008) 024002.

[9] SUTTROP, W., FUCHS, J. C., FISCHER, R., et al., Fusion Eng. Des. **88** (2013) 446.

[10] STRUMBERGER, E., GÜNTER, S., and TICHMANN, C., Nuclear Fusion **54** (2014) 064019.

[11] NÜHRENBERG, C., Phys. Plasmas **3** (1996) 2401.

[12] ANDERSON, D. V., COOPER, W. A., GRUBER, R., MERAZZI, S., and SCHWENN, U., Int. J. Supercomput. Appl. **4** (1990) 34.

[13] MERKEL, P. and SEMPF, M., Resistive wall modes of 3D equilibria with multiply-connected walls, in *Fusion Energy 2006*, (Proc. 21st Int. Conf., Chengdu, 2006) (Vienna: IAEA), CD-ROM file TH/P3-8, and http://www-naweb.iaea.org/napc/physics/FEC/FEC2006/html/index.htm, 2006.

[14] BOOZER, A. H., Phys. Fluids **25** (1982) 520.

[15] STRUMBERGER, E., MERKEL, P., TICHMANN, C., and GÜNTER, S., Linear stability studies in the presence of 3d wall structures, in *38th EPS Conf. on Plasma Phys.*, ECA Vol. 35G P5.082, Strasbourg, France, 2011.

[16] HUYSMANS, G. T. A., GOEDBLOED, J. P., and KERNER, W., Phys. Fluids B **5** (1993) 1545.

[17] KERNER, W., GOEDBLOED, J. P., HUYSMANS, G. T. A., POEDTS, S., and SCHWARZ, E., J. Comput. Phys. **142** (1998) 271.

[18] STRUMBERGER, E., GÜNTER, S., MERKEL, P., RIONDATO, S., and SCHWARZ, E., Nuclear Fusion **45** (2005) 1156.

[19] LÜST, R. and MARTENSEN, E., Z. Naturforschung **15a** (1960) 706.

[20] HIRSHMAN, S. P. and WHITSON, J. C., Phys. Fluids **26** (1983) 3553.

[21] HIRSHMAN, S. P., VAN RIJ, W. I., and MERKEL, P., Comput. Phys. Commun. **43** (1986) 143.

[22] NÜHRENBERG, J. and ZILLE, R., Equilibrium and stability of low-shear stellarators, in *Theory of Fusion Plasmas*, EUR 11336 EN, p. 3, Varenna, Italy, 1988, Proc. Joint Varenna-Lausanne Int. Workshop.

[23] HIRSHMAN, S. P. and MEIER, H. K., Phys. Fluids **28** (1985) 1387.

[24] KERNER, W., J. Comput. Phys. **85** (1989) 1.

[25] SUTTROP, W., GRUBER, O., GÜNTER, S., et al., Fusion Engineering and Design **84** (2009) 290.

[26] ROMIN, J. E., CAMPOS, C., ROMERO, E., and TOMÁS, A., SLEPc Users Manual, Technical report dsic-ii/24/02, Universidad Politecnica de Valencia, http://www.grycap.upv.es/selpc, 2014.

Appendix 1: Flux coordinate systems

Plasma and vacuum part of the CASTOR3D code are formulated for non-orthogonal 3D flux coordinates, and additionally, the original straight field line formulation is used. The latter holds only in case of axisymmetric equilibria.

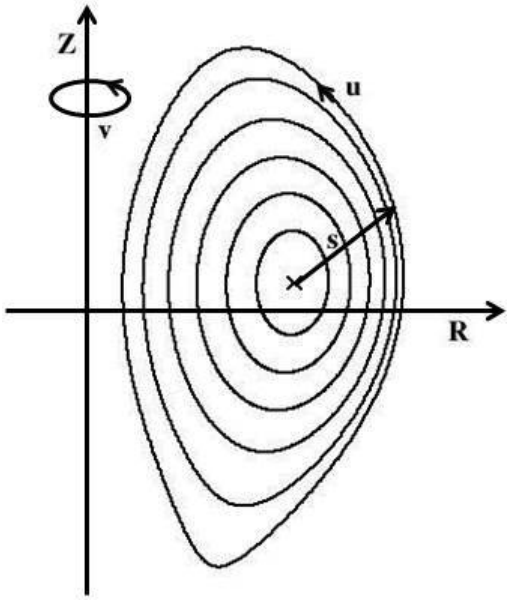

Fig.17: *Orientation of the flux coordinates used in the CASTOR3D code.*

The CASTOR3D uses the right-handed, non-orthogonal, flux coordinates (s, v, u). The radial coordinate $(0 \leq s \leq 1)$ labels the flux surfaces. It is defined as $s = \sqrt{\Phi/\Phi_{tot}}$ with Φ being the toroidal flux, and Φ_{max} being its maximum value. The toroidal $(0 \leq v < 1)$ and poloidal $(0 \leq u < 1)$ angle-like coordinates can be chosen arbitrarily, as long as the cylindrical coordinates (R, φ, Z) and the equilibrium magnetic field, $\vec{B}_0 = B^u \vec{r}_{,u} + B^v \vec{r}_{,v}$, are continuously differentiable functions of these coordinates.

Here three types of flux coordinates are used:

(i) NEMEC coordinates

The NEMEC code [20, 21] uses the coordinates (S, ξ, θ) where S is the normalized toroidal flux, and $\xi = \varphi$. The poloidal coordinate θ $(0 \leq \theta < 2\pi)$ is chosen in such a way that the Fourier representation of the flux surfaces is optimized [23]. The relations between CASTOR3D and NEMEC coordinates are: $s = \sqrt{S}$, $v = \xi/2\pi$, and $u = \theta/2\pi$.

(ii) Straight field line coordinates for axisymmetric equilibria

The original CASTOR code, which is restricted to axisymmetric equilibria, uses so-called straight field line coordinates $(s_{\rm pol}, \vartheta, \varphi)$. Field lines represented in these coordinates appear to be straight. The CASTOR3D code uses these coordinates with slight modifications. It uses

the square root of the normalized toroidal flux, s, instead of the square root of the normalized poloidal flux, $s_{\rm pol}$. Furthermore, it is $v = -\varphi/2\pi$, and $u = \vartheta/2\pi$.

These coordinates are implemented in two ways: (i) The matrix elements are used in the general 3D formulation, but they are computed for an equilibrium given in straight field line representation. (ii) The special forms of Jacobian and equilibrium field in these coordinates are explicitly used. Then, the matrix elements have a similar form as for the original CASTOR code [17].

(iii) Straight field line coordinates for 3D equilibria

The so-called Boozer coordinates (S, V, U) [14], which are used in the CAS3D [11] and STARWALL codes, are magnetic coordinates suitable for 3D equilibria. In this case, the matrix elements of the general 3D CASTOR3D formulation are calculated for an equilibrium represented in Boozer coordinates using: $s = \sqrt{S}$, $v = V$, and $u = U$.

Appendix 2: Representation of a coil

A coil is represented by an infinitely thin band which is discretized using triangles as shown in Fig. 18. The vertices of the triangles are located on the boundaries of the coil band. All vertices of one side are characterized by the same current potential. Usually, one potential is set to zero, while the other corresponds to the amount of the total current, I, flowing through the coil. Here, we define $\Phi_A = 0$ and $\Phi_B = I$.

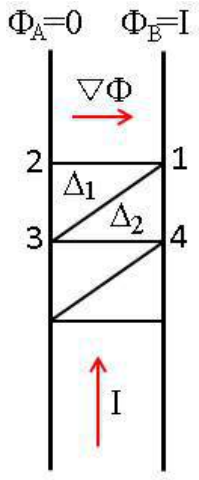

Fig.18: *Schematic representation of a coil segment.*

The postition vector of a triangle is given by

$$\vec{r} = \vec{r}_1 + \alpha\vec{r}_{2,1} + \beta\vec{r}_{3,1} \tag{54}$$

with $\alpha \geq 0, \beta \geq 0$, $0 \leq \alpha + \beta \leq 1$, $\vec{r}_{i,k} = \vec{r}_i - \vec{r}_k$, $i, k = 1, 2, 3$, and the vertices numbered anti-clockwise $(\vec{r}_1, \vec{r}_2, \vec{r}_3)$. Assuming the surface current density to be constant on a triangle,

$\vec{K}_\Delta$ is given by

$$\vec{K}_{\Delta_1} = \frac{\Phi_A \vec{r}_{2,3} + \Phi_A \vec{r}_{3,1} + \Phi_B \vec{r}_{2,3}}{|\vec{r}_{1,2} \times \vec{r}_{3,2}|} = \Phi_B \frac{\vec{r}_{2,3}}{|\vec{r}_{1,2} \times \vec{r}_{3,2}|} = I\vec{k}_{\Delta_1}, \tag{55}$$

$$\vec{K}_{\Delta_2} = \frac{\Phi_A \vec{r}_{4,1} + \Phi_B \vec{r}_{1,3} + \Phi_B \vec{r}_{3,4}}{|\vec{r}_{4,3} \times \vec{r}_{3,1}|} = -\Phi_B \frac{\vec{r}_{4,1}}{|\vec{r}_{4,3} \times \vec{r}_{3,2}|} = I\vec{k}_{\Delta_2}, \tag{56}$$

etc. That is,

$$\vec{K}_{\Delta_i} = I\vec{k}_{\Delta_i} \tag{57}$$

with $\vec{k}_{\Delta_i}$ being the normalized surface current density of triangle Δ_i.

Using this triangulization, for example, the third term of the Lagrangian $\mathcal{L}_{ideal}$ (39) reads

$$\frac{\mu_0}{8\pi} \sum_{n_c, n_c'=1}^{N_c, N_c} I_{n_c} I_{n_c'} \int_{S_{n_c}} df_{n_c} \int_{S_{n_c'}} df_{n_c'} \frac{\vec{k}_{n_c} \cdot \vec{k}_{n_c'}}{|\vec{r}_{n_c} - \vec{r}_{n_c'}|} \tag{58}$$

$$= \frac{\mu_0}{8\pi} \sum_{n_c, n_c'=1}^{N_c, N_c} I_{n_c} I_{n_c'} \sum_{i=1}^{N_{n_c}} \sum_{j=1}^{N_{n_c'}} \vec{k}_{\Delta_i} \vec{k}_{\Delta_j} \int_{S_{\Delta_i}} df_{\Delta_i} \int_{S_{\Delta_j}} df_{\Delta_j} \frac{1}{|\vec{r}_{\Delta_i} - \vec{r}_{\Delta_j}|},$$

where N_{n_c} is the total number of triangles representing coil n_c. For the explicit computation of the fourfold integral see [5].